JACS Au
AN OPEN ACCESS JOURNAL OF THE AMERICAN CHEMICAL SOCIETY

pubs.acs.org/jacsau
Article

Surface Structure to Tailor the Electrochemical Behavior of Mixed-Valence Copper Sulfides during Water Electrolysis

Avinava Kundu and Biswarup Chakraborty*

Cite This: JACS Au 2024, 4, 642−656
Read Online

ACCESS | Metrics & More | Article Recommendations | Supporting Information

ABSTRACT: The semiconducting behavior of mixed-valence copper sulfides arises from the pronounced covalency of Cu−S bonds and the exchange coupling between Cu^{I} and Cu^{II} centers. Although electrocatalytic study with digenite Cu_9S_5 and covellite CuS has been performed earlier, detailed redox chemistry and its interpretation through lattice structure analysis have never been realized. Herein, nanostructured Cu_9S_5 and CuS are prepared and used as electrode materials to study their electrochemistry. Powder X-ray diffraction (PXRD) and microscopic studies have found the exposed surface of Cu_9S_5 to be d(0015) and d(002) for CuS. Tetrahedral (T_d) Cu^{II}, distorted octahedral (O_h) Cu^{II}, and trigonal planar (T_p) Cu^{I} sites form the d(0015) surface of Cu_9S_5, while the (002) surface of CuS consists of only T_d Cu^{II}. The distribution of Cu^{I} and Cu^{II} sites in the lattice, predicted by PXRD, can further be validated through core-level Cu 2p X-ray photoelectron spectroscopy (XPS). The difference in the electrochemical response of Cu_9S_5 and CuS arises predominantly from the different copper sites present in the exposed surfaces and their redox states. In situ Raman spectra recorded during cyclic voltammetric study indicates that Cu_9S_5 is more electrochemically labile compared to CuS and transforms rapidly to CuO/Cu_2O. Contact-angle and BET analyses imply that a high-surface-energy and macroporous Cu_9S_5 surface favors the electrolyte diffusion, which leads to a pronounced redox response. Post-chronoamperometric (CA) characterizations identify the potential-dependent structural transformation of Cu_9S_5 and CuS to $CuO/Cu_2O/Cu(OH)_2$ electroactive species. The performance of the in situ formed copper-oxides towards electrocatalytic water-splitting is superior compared to the pristine copper sulfides. In this study, the redox chemistry of the Cu_9S_5/CuS has been correlated to the atomic arrangements and coordination geometry of the surface exposed sites. The structure−activity correlation provides in-depth knowledge of how to interpret the electrochemistry of metal sulfides and their in situ potential-driven surface/bulk transformation pathway to evolve the active phase.

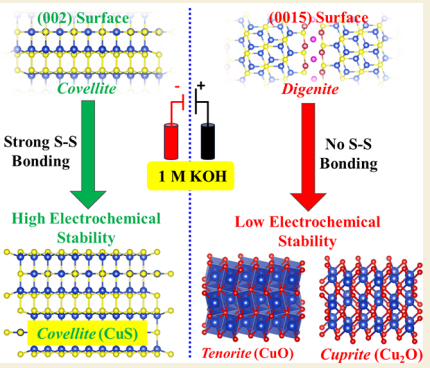

KEYWORDS: *mixed-valence, copper sulfides, lattice packing, surface-active sites, water-splitting, structure−activity correlation*

INTRODUCTION

Copper exists as a variety of sulfides, and the most common stoichiometric sulfide is chalcocite Cu_2S.[1,2] However, copper also forms a number of non-stoichiometric sulfides such as digenite (Cu_9S_5),[3] anilite (Cu_7S_4),[4] and yarrowite (Cu_9S_8),[5] and copper exists in mixed-valence states, namely, as Cu^{I} and Cu^{II}.[6] Although the sulfide ion (S^{2-}) is analogous to oxide (O^{2-}), the large ionic radius makes S^{2-} a soft donor, while the presence of a vacant d-orbital in S^{2-} is ideal to stabilize low-valence copper(I). Similar to peroxide (O_2^{2-}), disulfide dianion S_2^{2-} also exists and it is more stable than peroxide. Consequently, S_2^{2-} is found in the lattice structure of some copper sulfide like covellite CuS.[7] Due to strong covalent nature of the S−S bond in the S_2^{2-}, the presence of it in the lattice provides additional structural stability.[8] Profound covalency of the Cu−S bonds make the copper sulfide materials metallic or semiconducting in nature, which are ideal to study photovoltaic and/or electrochemical applications.[9,10] For an example, chalcocite Cu_2S is a p-type semiconductor due to its 1.2 eV band gap and is used as cathode material for Li-ion batteries.[11] Although covellite CuS is an example of stoichiometric sulfide, in the bulk lattice, trigonal planar (T_p) sites are preferably occupied by monovalent copper (Cu^{I}) ions and the divalent copper (Cu^{II}) ions are at the tetrahedral (T_d) sites.[12] In the close-packed structure, disulfide bonds are found in between two tetrahedral layers, which brings additional lattice stability.[10] Due to local non-homogeneity and imperfection in lattice packing, the non-stoichiometric copper sulfides possess a unique electronic structure, which gives an advantage in fabricating electrodes.[13] In this context, digenite Cu_9S_5 is a non-stoichiometric sulfide containing mixed-valence copper. However, controlling the phase purity during the preparation

Received: November 13, 2023
Revised: December 23, 2023
Accepted: December 28, 2023
Published: January 17, 2024

of nanoscale non-stoichiometric copper sulfides is not straightforward.[13]

Lately, copper sulfide nanomaterials have emerged as a potential alternative to noble metal-based material to fabricate electrodes.[14,15] Apart from a large abundance of copper, another reason to choose copper is that it possesses accessible redox states varying from Cu^{I} to Cu^{III}.[16] The electrochemical reactivity of copper sulfides arises from the redox active copper sites surrounded by S^{2-} ions, and the coordination geometry controls the redox potential of the material.[17] Under an applied potential and in the presence of alkaline electrolyte, copper sulfides are inherently unstable and sulfide leaching occurs to evolve copper oxide as electroactive species.[12] The electrode-potential-driven surface and bulk alteration have been referred to be the reason for the pronounced activity of the copper sulfide electro(pre)catalysts.[12,18] However, the lattice packing, surface structure, atomic arrangement of the exposed surface, surface energy, pH and concentration of electrolyte, and importantly applied potential bias are the controlling factors to determine the activity.[19] Some discrete studies are available in the literature where post-electrochemical characterizations were able to predict the reactive phase.[20] Although Cu_9S_5 and CuS are two examples of mixed-valence copper sulfides, they possess distinct lattice structures due to different types of atomic packing. They are not only structurally different, but also the ratio of Cu(I) to Cu(II) in the lattice and the arrangement copper sites in the exposed surface are distinct. Although electrochemical OERs with Cu_9S_5 and CuS have been recently studied,[12,18] no attempt to analyze the redox behavior of the mixed-valence copper sites and underlying reason for lattice instability under OER conditions has been made. However, the factors responsible for the electro-evolution and correlation of the activity to its electronic structure are necessary to understand. In this context, these two structurally distinct mixed-valence copper sulfide materials would be ideal candidates for a thorough electrochemical study. The correlation of their activity to the lattice structure or exposed surface sites can provide a detailed understanding of the plausible pathway of the electro-evolution of the sulfides to their active phase for the OER.

In this context, nanoscale particles of Cu_9S_5 and CuS are prepared solvothermally. The bulk morphology of the particles has been determined by microscopic studies and was found to be different. The lattice packing of rhombohedral for Cu_9S_5 and hexagonal for CuS are entirely different and contain a different ratio of Cu(I) and Cu(II) ions, as confirmed further by XPS studies. Cu_9S_5 contains less Cu(I) content compared to CuS, and their atomic arrangements in the lattice are entirely different. Apart from the higher percentage of Cu(I) in CuS, the lattice structure is further stabilized by a disulfide linkage.[8] The surface-exposed facets of these two nanoscale materials have been studied through high-resolution transmission electron microscopic (TEM) study and the atomic arrangement has been correlated from the PXRD data and reported crystal structure. A thorough electrochemical study is performed by depositing the materials on the electrode's surface and subsequent in situ Raman analyses to identify the electroactive species. Post-electrochemical study was further performed to characterize the electro-modified species. Combining the electro-modified electrodes obtained after chronoamperometric (CA) study at different polarities, an overall water-splitting cell was fabricated to produce green hydrogen with a fair Faradaic efficiency. In this study, the lattice structure, exposed surface facets and arrangement of redox sites in the reactive surface have been taken into consideration to interpret the electrochemical response of two mixed-valent copper sulfides.

RESULTS AND DISCUSSION

Lattice Structure of Digenite and Covellite

A one-step solvothermal reaction of a mixture of $CuCl_2$ (2.4 mmol) and Na_2S (2.8 mmol) in 2:1 ethylene diamine and water and heating at 200 °C for 5 h resulted in the isolation of crystalline digenite-phase Cu_9S_5. Recently, a single source precursor (SSP) approach was reported by Driess and co-workers to prepare phase-pure Cu_9S_5.[18] A dinuclear copper(I) complex stabilized by 2-mercaptopyridine was used as a precursor and was hot-injected to decompose at 250 °C to form digenite Cu_9S_5. Although the SSP method remains advantageous to control the growth of particles, a major shortcoming of the method is the additional step to prepare the pure precursor complex and the use of 2-mercaptopyridine as an expensive sulfur source. Comparatively, the single-step solvothermal approach using cheap copper(II) salt and a sulfur precursor led to the isolation of a pure digenite phase. The PXRD of the material provided well-defined reflections for (0015), (107), (1010), (0017), (110), and (1115) planes, highlighting the rhombohedral lattice of the Cu_9S_5 (ICDD: 00−047−1748) (Figure 1a) with space group $R\bar{3}m$ (166) and

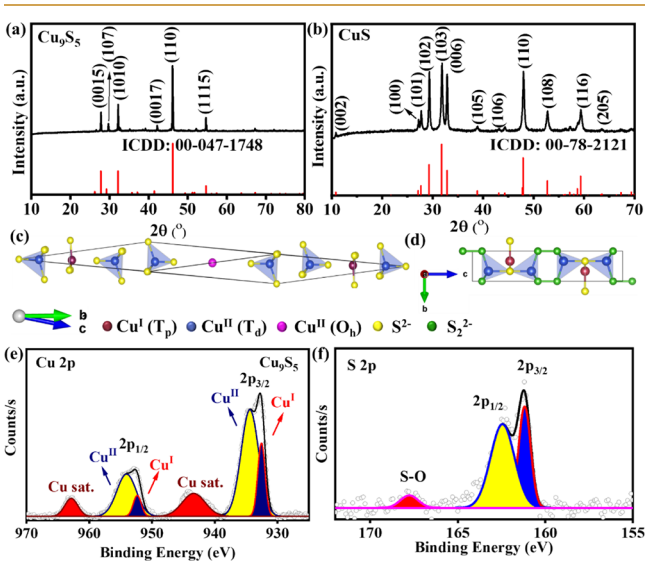

Figure 1. PXRD pattern for (a) digenite Cu_9S_5 and (b) covellite CuS along with the ICDD data (red bars). Atomic arrangement in the unit cell of (c) rhombohedral Cu_9S_5 and (d) hexagonal CuS. Deconvoluted core-level (e) Cu 2p and (f) S 2p XP spectra for Cu_9S_5, highlighting the spin−orbit components. The peak area of the Cu $2p_{3/2}$ spin−orbit components provided a Cu^{I} to Cu^{II} ratio of 2:7.06.

cell parameters a/b = 3.930 Å, c = 48.140 Å, and α/β = 90° and γ = 120°. One single unit cell contains multiple copper centers, and solid-state packing results in three different coordination geometries such as trigonal planar (T_p), tetrahedral (T_d), and octahedral (O_h) (Figure 1c).[9] The T_p sites are occupied by Cu^{I}, while the O_h and T_d sites are occupied by Cu^{II} species, and all the copper centers are connected through S^{2-} with μ_2 and μ_3 bridging motifs. In the T_p sites, the average Cu−S bond length is 2.249 Å. The T_d

https://doi.org/10.1021/jacsau.3c00703
JACS Au 2024, 4, 642−656

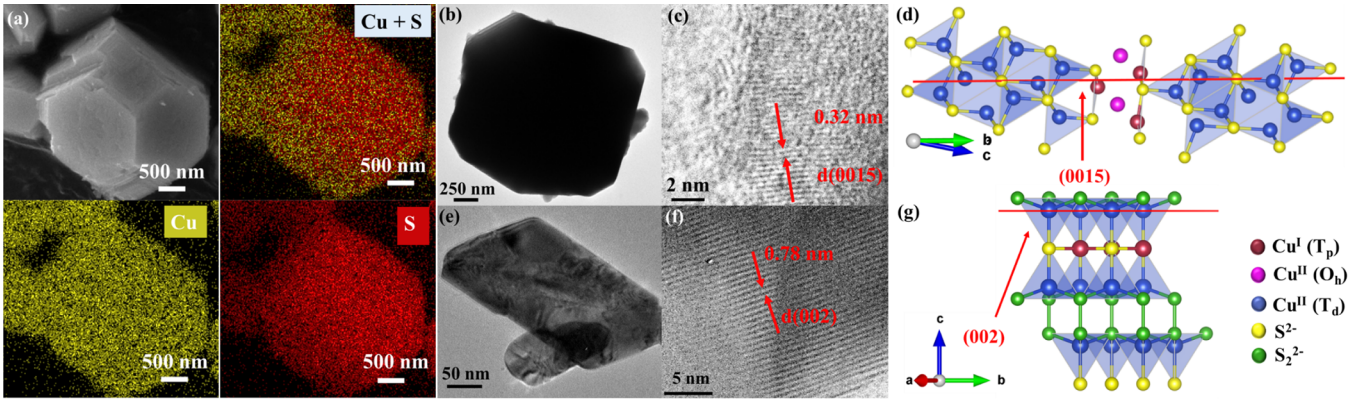

Figure 2. (a) FESEM image and EDX-elemental mapping of a single Cu_9S_5 particle (stacked Cu + S elements, Cu, and S). (b) TEM image of a single Cu_9S_5 particle, (c) high-resolution TEM image with d(0015) as exposed facets with a *d* spacing 0.32 nm, (d) lattice packing of rhombohedral Cu_9S_5 and atomic arrangements along the (0015) plane highlighted as a red line. (e) TEM image of an individual CuS particle, reproduced from *Inorg. Chem.* 2022, 61 (12), 4995−5009. Copyright 2022 American Chemical Society. (f) HR-TEM image with d(002) as exposed facets with a 0.78 nm *d* spacing and (g) atomic arrangement of CuS lattice along the (002) plane with exposed T_d Cu^{II} centers.

sites are partially distorted due to the presence of Cu(II), and one of the Cu−S bonds is more elongated and the length is 2.406 Å, while the rest of the three Cu−S bonds are shorter and are approximately 2.263 Å. The rhombohedral unit cell of the Cu_9S_5 possesses a significant number of O_h sites, which are occupied by Cu^{II}. A strong tetragonal distortion in the O_h Cu^{II} sites was observed with two axial Cu−S bonds to be 2.787 Å. In total, nine copper sites are present in the unit cell (Figure 1c) and are distributed as six $Cu^{II}S_4$ (T_d), one $Cu^{II}S_6$ (O_h), and two $Cu^{I}S_3$ (T_p). This typical arrangement of the Cu_9S_5 lattice results in a Cu^{II} occupancy of ca. 78% and ca. 22% Cu^{I}.

Similar to the digenite Cu_9S_5, covellite CuS is also a mixed-valent copper sulfide, and the hexagonal unit cell (Figure 1b) of the covellite comprises two different copper sites. In the solid-state structure (Figure 1d), two individuals tetrahedral (T_d) Cu^{II} units are bridged through a single sulfur atom with a Cu−S distance of 2.339 Å, while the other three Cu−S distances around the T_d Cu(II) centers are equal and have a value of 2.302 Å. The three-dimensional arrangement of the T_d sites allows us to locate trigonal planar (T_p) Cu(I) sites in between two T_d layers. The Cu−S distance around a T_p Cu(I) center is 2.192 Å, which is shorter than the Cu−S distance in Cu(II) sites. In the three-dimensional building unit of the covellite, disulfide linkages with a S−S distance of 2.094 Å contribute additional structural stability, holding two adjacent T_d layers of separate repeating units. The presence of a disulfide (S_2^{2-}) linkage resulted in a major structural difference in between covellite and digenite. However, both the copper sulfide structures contain mixed-valence copper centers, namely, Cu^{I} and Cu^{II}. Notably, the hexagonal unit cell (Figure 1d) of covellite contains 33% Cu^{I}, which is larger than that observed in rhombohedral Cu_9S_5.

The digenite structure of the synthesized material can further be established by XPS in which the core-level Cu 2p scan further supported the presence of mixed-valence copper states (Figure S1). Deconvolution of the core-level Cu 2p envelop depicted intense signals at 932.8 and 952.5 eV for the Cu $2p_{3/2}$ and Cu $2p_{1/2}$ spin−orbit components,[21] respectively, along with a spin−orbit (Δ2p) coupling component of 19.7 eV, which corresponded to the 22% Cu^{I} present in digenite.[18] In addition, the binding energy values observed in the Cu 2p envelop at 934.95 and 954.9 eV were assigned to the Cu $2p_{3/2}$ and Cu $2p_{1/2}$, respectively. The binding energy values of the Cu 2p spin-orbit components and the spin−orbit coupling of 19.95 eV can be assigned to the Cu^{II} present in the material (Figure 1e). The Cu 2p binding energy values and the spin−orbit components are well correlated to the covellite CuS structure[12] and other reported copper materials.[18,22] The core-level XP spectra of Cu_9S_5 also showed a strong band for S 2p. Deconvolution of the core-level S 2p displayed strong $2p_{3/2}$ and $2p_{1/2}$ spin−orbit components at 161.2 and 162.4 eV, respectively (Figure 1f), confirming the presence of S^{2-} in the structure. The presence of a weak signal at the 167.7 eV indicated the presence of S−O bond in the material presumably due to an aerial oxidation of Cu_9S_5 (Figure S1).[18,23] In addition to the Cu_9S_5 material studied herein, although the Cu 2p binding energies in the XP spectra of the covellite CuS is almost similar to those of digenite, the presence of disulfide $[S-S]^{2-}$ along with S^{2-} is distinctly visible in the core-level S 2p scan.[12] The Cu^{I} to Cu^{II} ratio identified from the X-ray crystal structure (from the reported CIF files) was further confirmed from the core-level Cu 2p XPS for both Cu_9S_5 and CuS samples. The Cu^{I} and Cu^{II} ratio present in Cu_9S_5 and CuS was calculated from the peak area of the deconvoluted Cu $2p_{3/2}$ spin−orbit components of Cu 2p envelops (Figure 1e and Figure S2). The calculated ratio of Cu^{I} to Cu^{II} from the XPS was 2:7.06 for the Cu_9S_5 and 2:3.8 for CuS, which can be well correlated to the ratio determined from XRD and/or reported data.[7,18]

The unequal distribution of Cu(I) and Cu(II) and the presence of different sulfide donors (S^{2-}, S_2^{2-}) affected the bulk morphology of these two mixed-valence copper sulfides. In the FESEM, the individual nanocrystal of the digenite material appeared as octagons with raptured edges and corners (Figure 2a), and the average edge dimension is ca. 1 μm (Figure S3). FESEM-EDX elemental mapping (Figure 2a) revealed an uniform distribution of Cu and S in the nanocrystal. The EDX spectrum recorded in a bulk area with numerous individual nanoparticles provided a Cu-to-S ratio of approximately 1.8, close to the theoretical ratio of Cu_9S_5 (Figure S4). The TEM image provided the individual octagon Cu_9S_5 nanocrystal in a two-dimensional projection (Figure 2b and Figure S5). The SAED pattern however confirmed the bulk crystallinity as revealed from the PXRD data (Figure S6). To elucidate the crystallinity of the octagonal-shaped Cu_9S_5 nanocrystals (Figure 2b), high-resolution TEM images were

https://doi.org/10.1021/jacsau.3c00703
JACS Au 2024, 4, 642−656

acquired and well-defined lattice fringes for (0015) planes (Figure 2c) were clearly visible near the edges of the individual nanocrystals. It could further be seen that, in Cu_9S_5, the (0015) planes are the exposed facet, which can behave as the reactive sites for catalysis.[18] The atomic arrangement of the (0015) planes (Figure 2d) of the Cu_9S_5 lattice found out that all three different copper centers, namely, O_h, T_d, and T_p, arranged themselves along the (0015) plane and all these sites are well exposed. Covellite CuS used herein for comparison possesses a nanoplate morphology (Figure 2e). The high-resolution TEM images revealed (002) planes as the most exposed facets (Figure 2f). Acquisition of HRTEM images in different regions or on different particles found dominantly the (0015) facets for the Cu_9S_5 and (006) facets (parallel plane of 002) for CuS (Figures S7 and S8). In the case of CuS, the planes corresponding to (002), (004), and (006) facets are parallel planes with different l values but the atomic arrangement is the same in these planes. HRTEM imaging of a randomly chosen single particle and selective illumination of (0015) (for Cu_9S_5) and/or (006) (for CuS) planes obtained in SAED study followed by acquiring dark-field HRTEM imaging revealed that Cu_9S_5 and CuS individual particles possess the most dominant exposed facets near the surface or edges of individual particles (Figures S9 and S10). The atomic arrangement in the hexagonal CuS infers that the (002) or (006) terminal is formed by only Cu^{II} T_d, while the Cu^{I} T_p centers are immediately below the exposed (002) surface (Figure 2g). In comparison to covellite's (002) exposed facet made off with only one type of copper center, the (0015) terminals of the digenite Cu_9S_5 are built up by T_d and O_h Cu^{II} centers and T_p Cu^{I}. Geometrical and valence-state disparity in the copper centers results in the (0015) surface of the digenite as a high-energy surface, which is anticipated to be more reactive compared to covellite.[24] However, in the covellite's (002) surface, the T_d Cu^{II} and T_p Cu^{I} centers in the first repeating layer is covalently linked to another layer by disulfide, which is apparently stronger than the Cu−S coordinate bonds. Given that, (002)-exposed covellite CuS can be more robust than the (0015)-exposed digenite under electrocatalytic conditions.[8,25]

The distribution of the different copper centers (O_h, T_d, and T_p) along the exposed (0015) plane of Cu_9S_5 leads to a high-energy surface. On the other hand, a periodic arrangement of T_d copper centers on the (002) or its congener (004) or (006) surfaces of the CuS make the exposed surfaces or edges of the particles relatively less energetic. A direct correlation to the surface energy can be drawn by understanding the interaction of the surface with liquid, preferably electrolyte, and gas. In practice, the contact-angle measurement using a liquid gives a fair idea about the surface energy. A high-energy surface in principle can rapidly adsorb liquid, and during the interaction, an acute contact angle is expected. On the contrary, when the energy of a surface is less, liquid adsorption will be comparatively less and an obtuse angle will be formed in the interface. In this context, to get a clear insight into the surface structure, the contact angle measurement was done with the thin film made of Cu_9S_5 and CuS powder samples using 1 M KOH as the liquid, which was used as electrolyte for the electrochemistry. The addition of 1 M KOH droplets on Cu_9S_5 and CuS film's surface resulted in contact angles (after exposure of 30 s) of 40° and 52°, respectively (Figure 3a). Real-time monitoring of the wettability from the time-resolved contact angle measurements (Figure 3b) using these two different surfaces revealed that the Cu_9S_5 surface adsorbed

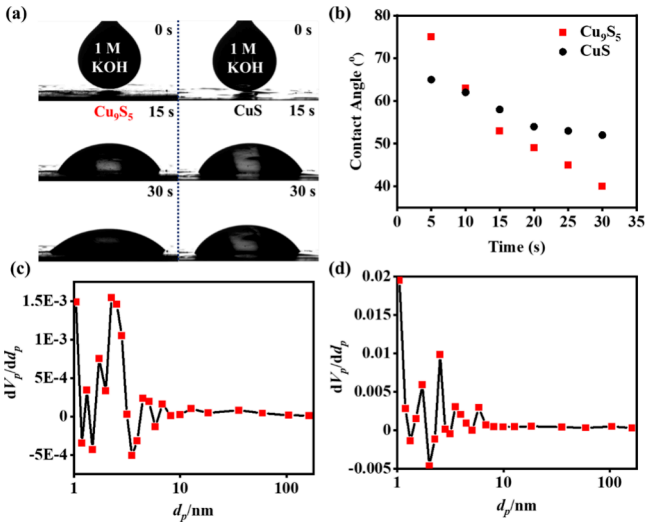

Figure 3. (a) Real-time images acquired at different time intervals (0 s, 15 and 30 s) during the casting of 1 M KOH droplet on the film prepared with Cu_9S_5 and CuS powder samples; (b) variation of the contact angle recorded during the wetting experiment of Cu_9S_5 and CuS with 1 M KOH droplet. Pore size distribution obtained from the BET study using N_2 at 77 K with (c) Cu_9S_5 and (d) CuS powder samples.

electrolyte at a much faster rate compared to the CuS surface. The extent of wettability by the surface gives a direct measure of its surface energy, and high-energy surfaces can be wetted more easily than low-energy surfaces.[26] Therefore, the contact angle measurement and wettability study affirmed that the Cu_9S_5 particle's surfaces are of high energy and presumably due to the distribution of different copper sites as described above.[27] The nitrogen adsorption−desorption isotherm (at 77 K) on Cu_9S_5 and CuS were further recorded to validate the variation in their surfaces. The physical adsorption−desorption of N_2 curves was recorded between 0 and 1 partial pressures. In the low-pressure region, the BET isotherm for Cu_9S_5 appeared to be rougher than that of CuS, which could be due to more roughness in the surface of Cu_9S_5 (Figure S11). Moreover, the Cu_9S_5 surface is composed of macropores dominantly, while multiporosity was observed for CuS (Figure 3c,d). BET data thereby further predicted a better electrolyte adsorption by the Cu_9S_5 surface.

Electrochemical Study with Cu_9S_5

Although the electrocatalytic activity with Cu_9S_5 was determined,[18,28] the electrochemical behavior of the copper sites located near the surface or bulk has never been explored. At first, the powder Cu_9S_5 was drop-casted on a 0.07 cm^2 surface area of a glassy carbon (GC) electrode with an approximate loading of 5.2 mg cm^{-2} and used as the working electrode. In a three-electrode cell setup using Pt as the counter electrode, Hg/HgO (1 M NaOH) as the reference electrode, and 1 M KOH as the electrolyte, the cyclic voltammetry (CV) was recorded within the potential range of 1.0 to −0.1 V (vs RHE). The CV scan was started at 1.0 V (vs RHE) and sweeped at a scan rate of 5 mV s^{-1} toward the cathodic direction to reach −0.1 V and moved back to the final potential of 1.0 V. In the cathodic wave of the first CV cycle, two dominant reduction peaks were observed at around 0.532 and 0.147 V. However, the redox peaks observed in the cathodic scan were too broad and ranged over a potential

https://doi.org/10.1021/jacsau.3c00703
JACS Au 2024, 4, 642−656

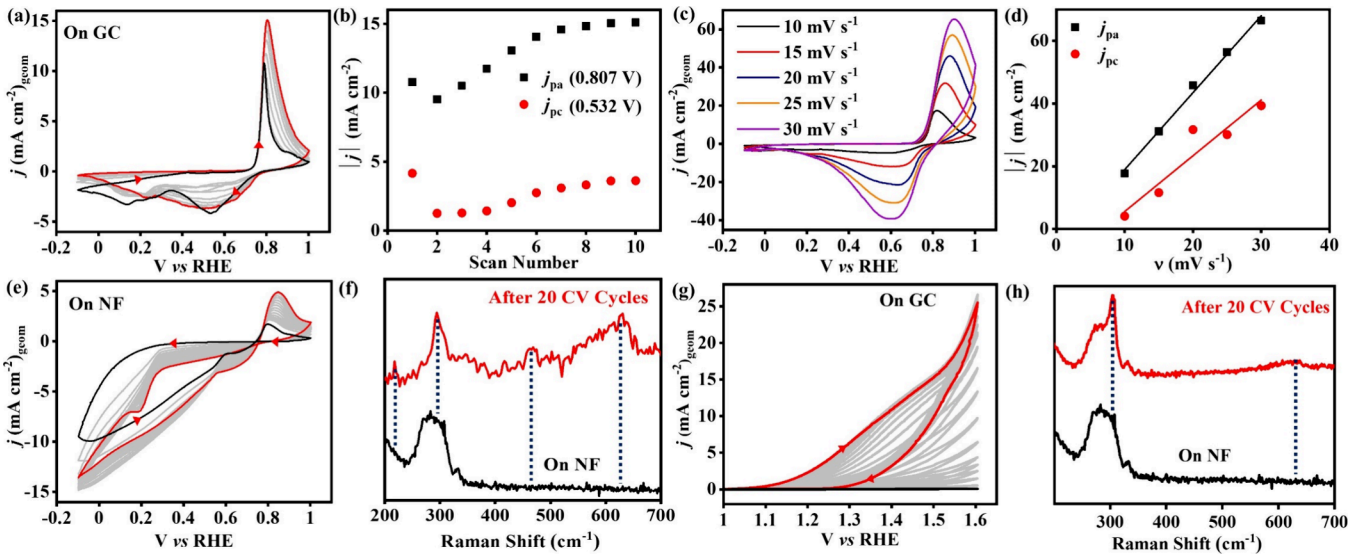

Figure 4. (a) Polarization curves from CV cycles obtained with Cu_9S_5@GC as a working electrode within a potential window of 1.0 to −0.1 V (scan rate of 5 mV s^{-1}; first scan (black) and last scan (red)); (b) change of the peak current density vs the number of scans, (c) CV cycles in different scan rates (inset: scan rate in mV s^{-1}), and (d) plot of peak current densities (|j|) vs the scan rate. (e) Polarization curves from CV cycles obtained for Cu_9S_5@NF as the working electrode within a potential window of 1.0 to −0.1 V (scan rate of 5 mV s^{-1}; first scan (black) and last scan (red)), (f) Raman spectra of the electrode before and after 20 CV cycles, (g) polarization curves from CV cycles obtained for Cu_9S_5@GC within 1.0 to 1.6 V (scan rate of 5 mV s^{-1}) and (h) Raman of Cu_9S_5@NF before (black curve) and after 20 CV cycles (red). Electrochemical condition: for panel a, c, and e, the scan starts at 1 V and the arrow indicates the direction of the scan; for panel g, the scan starts at 1 V with Pt as the counter electrode and Hg/HgO(1 M NaOH) as the reference electrode and 1 M KOH as the electrolyte.

window of 780 mV, corresponding to the reduction of Cu^{II} to Cu^{I} of distinct copper sites (Figure 4a).[29] The back (anodic) scan of the first CV cycle depicted a sharp redox peak at 0.807 V that can be assigned to the oxidation of reduced copper sites.[19] However, literature reports speculated that broadening of the current response in both anodic and cathodic scan can be attributed to the electrochemical responses of multiple copper sites adjacent to each other with comparable coordination geometry (Figure 4a).[19] Notably, the redox peaks in the first cathodic scan of the CV cycles were diffused and implied to multiple redox events within close potential values. A continuous broadening of the redox peaks in the cathodic waves was noticed in the subsequent CV cycles. With the progress of CV cycles, the cathodic peak current (j_{pc}) at 0.532 V dropped from its initial value of 4.5 mA cm^{-2}, and it reached almost a constant current after seven CV cycles (Figure 4b). More broadening of the redox peak in the cathodic scan was observed with the progress of CV cycles, which implied that more copper sites are participating in the reduction. Consequently, a gradual shift of the redox peak potential in the anodic scan was observed with an increasing number of cycles.[30] The diffused redox feature, peak shifting, and alteration of j_{pc}/j_{pa} with CV cycles are indicative of the structural modification of Cu_9S_5.[30]

As noted from the HR-TEM, the (0015) surface of Cu_9S_5 is well exposed, which consisted of three different copper sites, namely, Cu^{II} (T_d), Cu^{II} (O_h), and Cu^{I} (T_p). This atomic arrangement with differently exposed copper sites leads to different redox potentials.[31] Thus, it is presumed that the presence of different copper centers would come up with different electrochemical responses. The diffused redox peaks in the cathodic scan can be correlated to the (0015) exposed facet of Cu_9S_5 where different coordination geometries and different valence states of the copper centers are presumably responsible for the diffused redox response in a close potential window. The variation of the scan rate plays a crucial role in understanding the potential-induced chemical changes occurring in the catalyst on the electrode surface. CV scans with varying scan rates provided an almost linear relationship with the peak current and scan rate (Figure 4c,d). However, with the increase of the peak current, a peak (j_{pc}) to peak (j_{pa}) separation was dominated, which may lead to a pronounced quasi-reversibility of the $Cu^{II/I}$ redox process.[32] At a higher scan rate ($\nu \geq 20$ mV s^{-1}), in the cathodic scan, the peak current became more diffused, and no redox current was apparent in the 0.3 to −0.1 V region. The electrochemical response in the low scan rate (5−15 mV s^{-1}) is more sensitive to the diverse copper sites in the surface. However, the dynamic polarograms in the CV studies inferred a chemical alteration in the structure, which presumably passivates from the surface to bulk.[33] The electrode substance plays a crucial role in electrochemical behavior. Nickel foam is always chosen due to its capability of a high mass loading and preferable electronic conduction.[34] An additional advantage of depositing Cu_9S_5 on NF was to spectroscopically study the material under quasi in situ conditions. During the electrochemical studies, an ∼5 mg mass loading of Cu_9S_5 was maintained to achieve the best activity (Figure S12) for both the hydorgen evolution reaction (HER) and oxygen evolution recation (OER). A mass loading of 5 mg of Cu_9S_5 on NF and subsequent CV study in identical three-electrode cell within the same potential window resulted in a non-redox current response until 0.2 V (vs RHE), while a large catalytic current (j: 9.78 mA cm^{-2}) was received on moving toward −0.1 V (Figure 4e). Reverse scan of the first cycle showed a large current response and crossed the cathodic scan at 0.7 V followed by redox feature at 0.811 V for the $Cu^{I/II}$ couple. In the cathodic scan, the catalytic current was indicative of HER, while the crossover in the backward scan is implying a chemical change associated with an electron transfer reaction.[35] Notably, with the progress of CV cycles a

https://doi.org/10.1021/jacsau.3c00703
JACS Au 2024, 4, 642−656

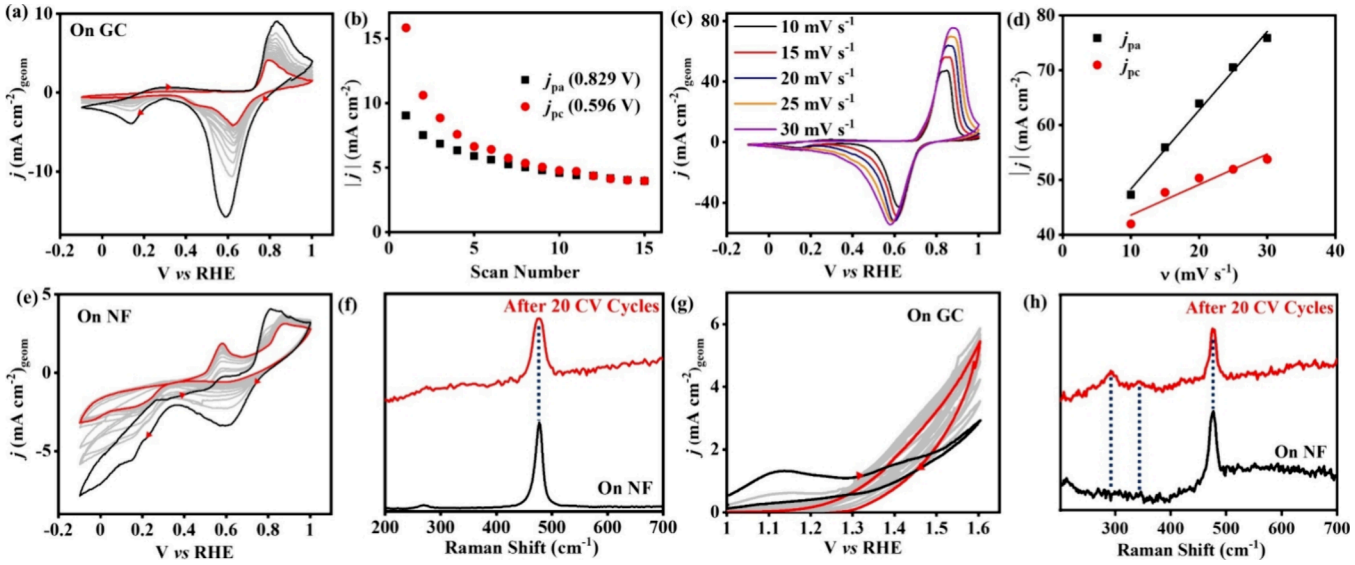

Figure 5. (a) Polarization curves from CV cycles obtained with CuS@GC as the working electrode within a potential window of 1.0 V to −0.1 V (scan rate of 5 mV s^{-1}, first scan (black) and last scan (red)), (b) change of the peak current density vs the number of scan, (c) CV cycles in different scan rates (inset: scan rate in mV s^{-1}), and (d) the plot of peak current densities ($|j|$) vs the scan rate. (e) Polarization curves from CV cycles obtained for CuS@NF as the working electrode within the potential window of 1.0 V to −0.1 V (scan rate of 5 mV s^{-1}, first scan (black) and last scan (red)). (f) Raman spectra of the electrode before and after 20 CV cycles. (g) Polarization curves from CV cycles obtained for CuS@GC within 1.0 to 1.6 V (scan rate of 5 mV s^{-1}) and (h) Raman of CuS@NF before (black curve) and after 20 CV cycles (red). Electrochemical condition: for panel a, c, and e, the scan starts at 1 V and the arrow indicates the direction of the scan; for panel g, the scan starts at 1 V with Pt as the counter electrode and Hg/HgO(1 M NaOH) as the reference electrode and 1 M KOH as the electrolyte.

redox feature at 0.195 V became prominent, which can be ascribed to the reduction of different Cu^{II} sites. The large background current within the 0.6 to 0.3 V can presumably be due to reduction of the surface-exposed O_h and T_d Cu^{II} sites. In the literature report, the Cu^{I} has been implicated as the key reactive species and herein the CV study can directly identify the formation of Cu^{I}. However, a gradual increase in the cathodic current response followed by the crossover of the backward scan (anodic direction) and peak shift of $Cu^{I/II}$ couple were combined, inferring the chemical alteration of the Cu_9S_5. Under quasi in situ conditions, Raman study with the Cu_9S_5 deposited NF electrode found out that the Raman band at 284 cm^{-1}, which is characteristic for the Cu−S vibration of Cu_9S_5, was missing after 20 CV cycles and the appearance of the new set of Raman bands can be assigned to Cu_2O (219 cm^{-1}, 624 cm^{-1}), CuO (302 cm^{-1}, 489 cm^{-1}), and $Cu(OH)_2$ (292 cm^{-1}) (Figure 4f).[19] In a recent study by Kim et al., copper sulfide was shown to form Cu_2O as a reactive species under the nitrogen reduction conditions in 0.5 M Na_2SO_4 medium.[22]

CV performed within 1.0 V to −0.1 V in 1 M KOH and subsequent quasi in situ Raman study identified the electrochemical instability of Cu_9S_5. The electrochemical behavior of Cu_9S_5 was further explored in an anodic potential window, namely, 1 to 1.6 V, traditionally performed for electrocatalytic OER study. Driess and co-workers recently reported Cu_9S_5 prepared from a molecular precursor using the SSP approach as a potential OER catalyst.[18] However, a detailed electrochemical study to identify the redox behavior of the copper sites and their influence in the catalytic OER was not performed. A careful analyses of the redox response of Cu_9S_5 within the 1−1.6 V (Figure 4g) potential window gave a scope to detect the transient high-valent copper species involved in the OER. The first CV cycle with Cu_9S_5 on GC neither showed any detectable redox peak nor the catalytic current. However, with the progress of CV cycles, a redox peak became prominent after 1.1 V. After seventh CV cycle, the catalytic current was visible after 1.3 V. A high catalytic current of 27 mA at 1.6 V after 20 CV cycles is seen in Figure 4g. Increasing the current with CV cycling denoted an activation of the catalyst as documented for CuS and Cu_2S.[20] A prominent redox feature within 1.22 to 1.51 V was clearly visible in the twentieth CV cycle. The redox feature with a $E_{1/2}$ value of 1.36 V can presumably be assigned to the formation of Cu(III) transient species[36] to catalyze the OER, which was evident from the catalytic current appearing immediately after the redox region (potential >1.5 V). CV study on NF was comparable to that observed with GC and reported earlier.[18] However, NF provided an opportunity to study Raman under quasi in situ conditions. The Raman spectrum of the electrode after 20 CV cycles within 1.0−1.6 V resulted in a sharp band at 309 cm^{-1} and a broad band at 610 cm^{-1}, emphasizing the formation of CuO and $Cu(OH)_2$ under the catalytic conditions (Figure 4h).[19] The presence of the characteristic Cu−S Raman band in the post CV cycle Raman spectrum highlighted that copper oxides were generated at the surface while the bulk remained unaltered. Long-term chronoamperometry (CA) with Cu_9S_5 deposited on NF and subsequent ex situ analyses inferred the formation of a CuO@Cu_9S_5 core−shell.[18] The appearance of a redox peak around 1.4 V for $Cu^{II/III}$ pointed out that the Cu^{III} transient species formed at the surface of Cu_9S_5 during the OER. In alkaline medium and under an anodic potential, surface-exposed Cu^{II} sites may undergo rapid hydroxylation to $Cu(OH)_2$, which can spontaneously loose water to form CuO. Under the anodic potential, the Cu^{III} species is generated as a transient catalytic intermediate.[36] In a recent study, the anodic oxidation of Cu(II) to Cu(III) has been proposed to be involved in the OER, which has been spectro(electro)chemically detected.[19,20] The (0015) facets are the exposed lattice planes for Cu_9S_5 and

https://doi.org/10.1021/jacsau.3c00703
JACS Au 2024, 4, 642−656

the different copper sites present in the (0015) planes played an intriguing role in controlling the formation of reactive species. Under an applied anodic potential, hydroxylation of O_h copper(II) sites is more likely as they are in a highly distorted O_h geometry and possessing a tetragonal distortion with two long axial Cu−S bonds. After hydroxylation of a single Cu^{II} (O_h) site, surface corrosion (hydroxylation) may slowly propagate and sulfide leaching from the surface will occur to generate a thin layer of copper oxide. A similar observation was documented for covellite and other transition metal sulfide materials.[12,37−39] Also, in another study, degradation of iron pyrite was noticed under electrochemical conditions where the presence of perchlorate and a proton source accelerate the structural alteration.[40] The wettability test performed with the Cu_9S_5@NF electrode after 20 CV cycles in two different potential regions inferred that, after anodic activation, the surface become hydrophilic due to surface rupturing and better diffusion of electrolyte (1 M KOH) was observed (Figure S13). On the contrary, the extent of surface wettability after cathodic activation of the Cu_9S_5@NF is comparatively less (Figure S13). As a consequence, a structural alteration of Cu_9S_5 under anodic conditions was predominant.

Electrochemistry of CuS and Comparison with Cu_9S_5

The atomic arrangement in the hexagonal CuS lattice depicted that the terminal of the (002) exposed surface consisted of T_d $Cu^{II}S_4$ sites (Figure 2g), which is completely different than the (0015) surface of Cu_9S_5. Additionally, a strong disulfide linkage $(S-S)^{2-}$ holds two independent $Cu^{II}(T_d)$-$Cu^{I}(T_p)$-$Cu^{II}(T_d)$ layers (Figure 2g). Despite a large structural dissimilarity of the covellite CuS with digenite Cu_9S_5, they are electronically related due to the presence of mixed-valence copper in the lattice. However, a notable difference is the composition of Cu^{I} to Cu^{II} in the lattice and distribution of Cu^{I} to Cu^{II} in the exposed surfaces. Given the structural and chemical disparity, it is expected to observe a change in the redox response. The electrochemical behavior of CuS was therefore studied in an identical condition within the similar potential window and comparable mass loading on the GC electrode (Figure 5a). The first polarization curve obtained from the CV cycles depicted two distinct redox waves. The cathodic scan of the first CV cycle showed a redox peak at 0.596 V with a predominant cathodic peak current (j_{pc}) of 15.1 mA, which can be assigned to the single-electron reduction of T_d Cu^{II} sites present in the (002) surface.[29] The broad and weak redox peak at 0.134 V can be assigned to the reduction of chemically different Cu^{II} sites presumably from the inner-layer copper sites (Figure 2g).[29] In the reverse scan, the well-resolved redox peak at 0.829 V is in accordance with the reoxidation of Cu^{I} to Cu^{II}.[19] However, an almost 233 mV peak to peak separation of the reduction and oxidation wave demonstrate that the reduction of Cu^{II} to Cu^{I} is associated with a partial chemical alteration in the surface. With the progress of CV cycles, the peak current in both cathodic and anodic wave diminished significantly and stable wave was observed after 15 CV cycles (Figure 5b). Notably, a diminished current of the second cathodic wave and a small anodic shift were also in accordance with the partial modification of the copper sites during redox process. Further, the CV study with varying scan rates revealed a linear relationship with the j_{pc} and j_{pa} with the scan rate (ν) (Figure 5c,d).[32] CV studies thereby highlighted that T_d Cu^{II} terminals at the (002) surface depict redox activity during the CV cycles and the copper sites of the bulk are apparently not participating. Electrochemical data further emphasized, that in comparison to the (002) facet-exposed CuS, the (0015) exposed Cu_9S_5 material appears to be labile under CV cycles, and in situ reconstruction of Cu_9S_5 to the oxidic phase induced by CV cycling was dominated to affect the bulk structure. It could be noted that the (002) surface of CuS has a regular arrangement of T_d Cu^{II} sites, while the (0015) surface of the Cu_9S_5 has T_d Cu^{II}, T_p Cu^{I}, and O_h Cu^{II} sites and plausibly the presence copper sites with three different coordination environment make the (0015) surface more electro-sensitive with diffused electrochemical responses from the different copper centers. In contrary, the electrochemical response for CuS was more distinct and appeared from the surface T_d Cu^{II} sites.

To validate the bulk stability of covellite and $Cu^{II/I}$ redox from the T_d Cu^{II} sites only of the (002) surface, the electrochemical behavior of CuS deposited NF (Figure 5e) was tested along with quasi in situ Raman study of the electrode. The first CV cycle recorded (1.0 V to −0.1 V) with CuS@NF showed an identical redox feature of $Cu^{II/I}$ at around 0.6 V. Beyond 0.4 V, a large cathodic current indicated the catalytic HER. However, before the catalytic current, the dominant redox feature at 0.6 V was apparent and can be assigned to the reduction of Cu^{II} to Cu^{I}, which perhaps catalyzes the HER. In subsequent CV cycles, both the redox feature in the cathodic scan become less dominant along with diminishing the catalytic current between 0.4 and −0.1 V. Notably, in the anodic back scans, two oxidation peaks appeared and indicated the reoxidation of the electro-generated Cu^{I}. The broad redox peak in the cathodic scan and two visible redox peaks in the anodic scan were indicative of multiple copper sites involved in the redox process. The Raman spectrum of the electrode recorded immediately after 10 CV cycles showed a prominent band at 476 cm^{-1} characteristic (Figure 5f) for the S−S (S_2^{2-}) vibration of pristine covellite and inferred an unaltered bulk structure. An undetectable surface reduction is precedent from the anonymous redox feature on NF. It could be due to the background redox effect of NF being a non-innocent electrode substance. However, during the CV cycles within 1.0 to 1.6 V (vs RHE), the clear redox feature on GC and the Raman data after CV (Figure 5g,h) cycles affirmed a partial modification of the covellite within the potential window of 1.0 to 1.6 V and in 1 M KOH. Apart from the strong characteristics Raman band at 476 cm^{-1} for the S−S interlayer of the CuS, two weak Raman signals at 300 and 350 cm^{-1} appeared due to the oxidation of the surface layer to CuO via sulfide leaching pathway.[12,38] Surprisingly, under the same electrochemical conditions, Cu_9S_5 appeared to be more labile compared to CuS, and surface corrosion to bulk alteration was noticed. It is specifically due to the surface inhomogeneity of Cu_9S_5 along the (0015) plane that led to structural lability, whereas the homogeneously distributed Cu^{II} centers along the (002) plane along with stronger S−S interlayer bonding provided structural rigidity to CuS. The better stability of the crystal packing restricted facile transformation into CuO and/or $Cu(OH)_2$. The rapid increase in the redox peak intensity at 1.4 V in the CV cycles of Cu_9S_5 between 1.0 and 1.6 V (Figure 4g) confirmed the formation of Cu(III) species through structural disintegration. Meanwhile, in comparison to Cu_9S_5, the CuS did not show any distinct formation of Cu(III) species at a

https://doi.org/10.1021/jacsau.3c00703
JACS Au 2024, 4, 642−656

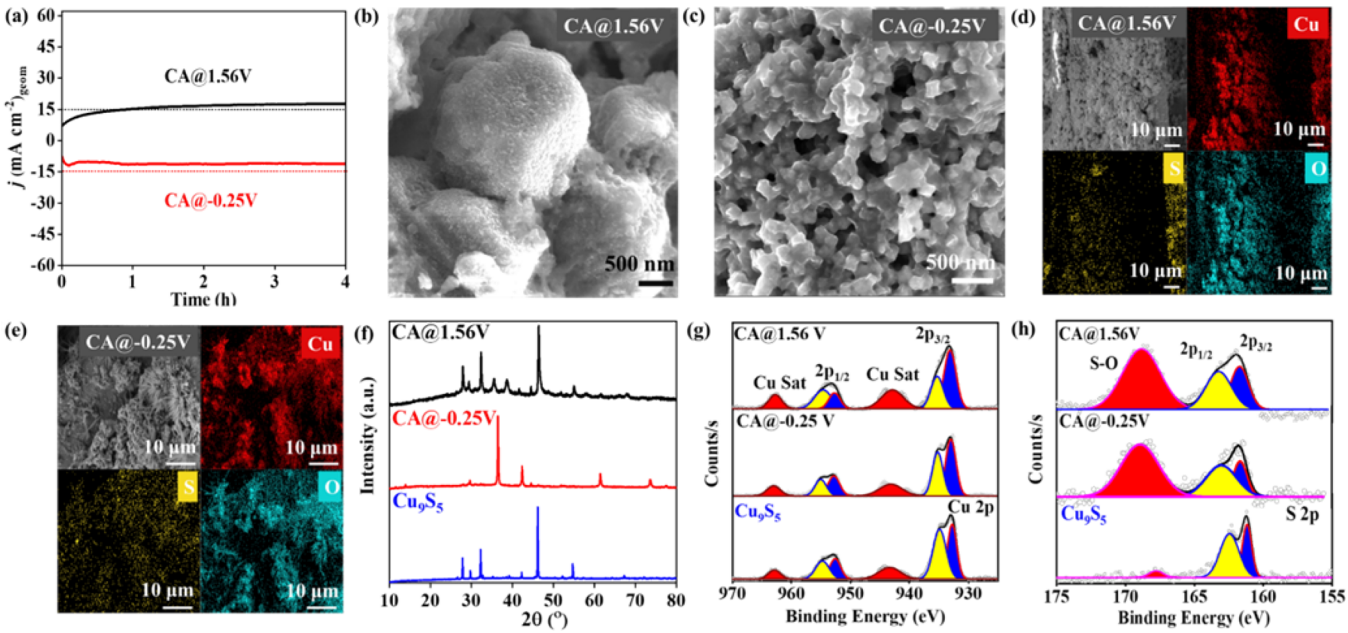

Figure 6. (a) Chronoamperometry (CA) study performed with Cu_9S_5@NF under an applied potential of 1.56 V (black) and −0.25 V (red) vs RHE. High magnification FESEM images after CA at (b) 1.56 V and (c) −0.25 V vs RHE for 4 h. FESEM-EDX elemental mapping after electrolysis at (d) 1.56 V and (e) −0.25 V vs RHE. (f) Powder XRD pattern of pristine Cu_9S_5 (blue), after CA@-0.25 V (red) and after CA@1.56 V (black). Core-level (g) Cu 2p and (h) S 2p XP spectra of pristine Cu_9S_5, after CA@-0.25 V and after CA@1.56 V.

similar potential. Therefore, among the two different copper sulfides, the ease of $Cu^{II/III}$ transformation led to higher catalytic activity for Cu_9S_5, which is evident from a better catalytic current response at 1.6 V (Figures 4g and 5g) than CuS.

Chronoamperometry and Bulk Structural Alteration

During CV cycling, rupturing of the Cu_9S_5 structure was precedent, which was indicated by quasi in situ Raman study. To characterize the bulk material by various microscopic techniques, CA studies were conducted under two extreme constant potentials, namely, −0.25 and 1.56 V (vs RHE) (Figure 6a). As noted, a −0.25 V potential is more negative to the observed reduction potential of $Cu^{II/I}$ in Cu_9S_5, while 1.56 V is above the oxidation potential of $Cu^{II/III}$.[31] It is expected that, under these two CA conditions, the charge passing through the electrode will initially be used for the bulk redox change of the structure.[41] For the initial 1.5 h of CA, a fluctuation in the amplitude of current density ($|j|$ mA cm^{-2}) was noticed along with a slow rise in the average current density with time, which can be ascribed to the chemical alteration in the catalyst associated with the redox change.[22] The gradual increase in the current further indicated that the modification in the Cu_9S_5 structure accelerated its electrochemical performance. Almost after 2 h of CA at both the potentials, the delivered current density become constant at 14.6 mA cm^{-2} (for CA at 1.56 V) and −13.5 mA cm^{-2} (for CA at −0.25 V), respectively. After CA at 1.56 V, the FESEM images showed rupturing of the octagonal particles. The smoothness of the particles' is severely affected, and the surfaces became rough, which is indicative of a partial breakdown of the surface to several nanometers in depth to give a reactive copper oxide shell (Figure 6b and Figure S14). However, after 4 h of CA at −0.25 V, the morphology of the particle identified in the FESEM image was entirely different and they appeared as 80−120 nm particles (Figure 6c and Figure S15). FESEM−EDX mapping identified a huge sulfide loss from the particle and incorporation of a significant amount of oxygen in the structure (Figure 6d,e and Figures S16 and S17). To identify further the species generated under two extreme potentials, PXRD of the isolated materials from the electrode after CAs were recorded. PXRD depicted that, after CA at 1.56 V, few new reflections arose along with the desired reflections for Cu_9S_5 (Figure 6f and Figure S18). Indexing of the new reflections found that a significant amount of CuO is formed on Cu_9S_5 during 4 h of CA and the source of oxygen found in the FESEM-EDX can now be correlated to CuO. The TEM image of the particle also revealed ruptured surfaces of individual nanoparticles (Figure S19a,b), while the high-resolution TEM identified lattice fringes for (11−1) of CuO near the edges (Figure S19c) confirm a core−shell arrangement of CuO@Cu_9S_5 similar to that reported earlier with Cu_9S_5.[18] The SAED pattern further revealed the reflection of the (1010) plane of the Cu_9S_5 core and (11−1) planes (Figure S19d) from the CuO shell (Figure S19d). After CA, at −0.25 V, the material was also isolated from the electrode and analyzed by PXRD. Surprisingly, the reflections of pristine Cu_9S_5 were absent and a new set of reflections appeared due to Cu_2O (Figure 5f). As noted in the FESEM-EDX elemental mapping, the source of sulfur can be assigned to leached sulfide readsorbed to the surface, which does not show any reflections in PXRD.[42] The TEM images of the material isolated after CA under cathodic conditions (at −0.25 V) showed nanoparticles of much smaller dimension (300 × 280 nm) than that of the pristine Cu_9S_5. A close look to the surface of the particles revealed an amorphous layer almost in all particles, which presumably could be for the CuO formed due to surface passivation of Cu_2O (Figure S20a,b).[12,20] The well-resolved lattice spacing for d(110) planes of Cu_2O is seen in the HR-TEM (Figure S20c). The SAED pattern depicted bright spots of (110), (200), and (220) (Figure S20d), which further

https://doi.org/10.1021/jacsau.3c00703
JACS Au 2024, 4, 642−656

confirmed the crystallinity of active Cu_2O formed under −0.25 V CA conditions via bulk alteration of Cu_9S_5.

XPS study was further performed with the materials isolated after CAs, and an elemental scan in XP spectra found a strong peak of oxygen along with copper and sulfur (Figures S21 and S22). Core-level Cu 2p and S 2p was analyzed to correlate the surface and bulk alteration of Cu_9S_5 under CA at +1.56 V and −0.25 V, respectively. The comparison of the binding energies of the spin-orbit component of Cu 2p corresponded to the presence of Cu^I and Cu^{II} in post CA samples (Figure 6g). As proven by other spectroscopic studies, Cu_9S_5 transformed to CuO-Cu_9S_5 under the anodic CA condition (at +1.56 V),[43] which is likely to see the coexistence of Cu^I and Cu^{II} and XP spectrum for Cu 2p supporting the presence of mixed-valence copper (Figure 6g).[28] Further, the prominent core level S 2p (Figure 6h) envelop within the binding energy values of 160−164 eV is due to S^{2-} and S_2^{2-} from the core Cu_9S_5. Along with that, the dominant signal at 168 eV can be ascribed to S−O of sulfate re-adsorbed on the surface and it was formed due to oxidation of the leached S^{2-} in alkaline medium and under anodic conditions.[12] After electrolysis at 1.56 V versus RHE and −0.25 V versus RHE, the SO_4^{2-} anion was detected via a qualitative wet-test, which affirmed the leaching of sulfur ions from the Cu_9S_5 for the electrochemical reconstruction (Figures S23 and S24). However, in the Cu 2p XP spectrum of the material isolated after −0.25 V CA for 4 h, the presence of Cu^I and Cu^{II} was predominated from the binding energy values (Figure 6g). It is well correlated to the HRTEM figures as a thin amorphous layer of CuO formed on Cu_2O, which was electrochemically derived from the Cu_9S_5. It could further be noted that, in the S 2p spectrum, an intense peak of S−O along with a notable peak for S^{2-} was observed, which are due to re-adsorbed sulfur species commonly seen in the metal sulfide electro(pre)catalyst.[42] Apart from Cu 2p and S 2p, both the materials isolated under different CA conditions showed a strong O 1s signal and the deconvoluted core-level O 1s spectra are well apprehended with O^{2-}, which is in line with the formation of CuO and Cu_2O under the electrochemical conditions.

After the ex situ post-characterizations with the Cu_9S_5@NF electrode obtained after 4 h CA at −0.25 and 1.56 V (vs RHE), in situ Raman study was performed with in-house customized cell (Figure S25)[19,44] to detect the transient active species during the electrochemical studies.[45−47] During the CA at −0.25 V (vs RHE), Raman spectra were recorded with a short time interval. Raman spectra acquired after 300 s of CA revealed a strong Raman band at 162 cm^{-1}, which could be assigned to the formation Cu_2O. The weak band at around 302 cm^{-1} observed can be due to the formation of CuO species (Figure S26). However, no further change in the Raman spectra was noticed with the progress of CA for another 10−15 min (Figure S26). The ex situ Raman data recorded with the Cu_9S_5@NF after 20 CV cycling has also identified the formation of Cu_2O and CuO. Thereby, both the ex situ and in situ Raman study pointed out an electrochemical transformation of Cu_9S_5 to CuO-Cu_2O to facilitate the HER. Using the same setup, 20 CV cycles within the potential range of 1.0−1.60 V (vs RHE) were performed with a Cu_9S_5@NF electrode and the electrode showed a distinct Raman band at 301 and 592 cm^{-1} for CuO and 476 cm^{-1} for $Cu(OH)_2$. However, after CA at 1.56 V for 300 s resulted in the formation of Cu_4O_3, an unstable transient species showed its characteristic Raman band at 552 cm^{-1}.[48] $Cu(OH)_2$ bands were visible and remained even after 10 min of CA (Figure S27). Notably, Cu_4O_3 is also mixed-valence copper oxide where both Cu^I and Cu^{II} are present. Therefore, the formation of this transient copper oxide species, namely, CuO or $Cu(OH)_2$, can be the electro-generated active species for the OER.

As evident, the coordination environment of the exposed metal sites in a material played a pivotal role in providing a good structural stability and/or the lattice stability under electrocatalytic conditions. Based on the redox features of the CV cycles, in situ spectroscopic data and subsequent post CA characterization confirmed the structural alteration of Cu_9S_5 under two different electrode polarities and it appeared as more labile compared to CuS. However, the electrochemical lability of Cu_9S_5 allows us to generate the electroactive species to catalyze water splitting. The nature of the electroactive species formed under the potential conditions depends on several factors such as the pH, nature of the electrolyte, concentration of the electrolyte, composition of the catalyst, its lattice stability, exposed facet, and its surface energy and importantly the applied bias potential. The lattice structure and exposed facet analysis provided some clue to interpret the electrochemical response and subsequent electrochemical in situ modification of these two mixed-valent copper sulfides chosen herein. Sulfide leaching followed hydrolytic dissolution under the applied potential has been inferred as the common pathway of metal sulfide to evolve the reactive oxidic phase directly on the electrode surface.[38,39] Based on the electrochemical and post CA analyses, Cu_9S_5 follows a common pathway to evolve into the CuO-Cu_2O active species. However, the sulfide leaching is anticipated to begin at the (0015) surface. Most likely, the highly distorted O_h Cu^{II} sites on the surface first undergo hydrolysis to form $Cu(OH)_2$, which then, under applied potential conditions, propagates smoothly to other surface sites and finally to bulk sites (Scheme 1).

Scheme 1. Surface (Red Arrow in Left) versus Bulk Alteration (Black Arrow in Right) of the Pristine Cu_9S_5 (Ball and Stick Representation at Center) under Two Chronoamperometric Conditions: CA @ 1.56 V and CA @ −0.25 V; Surface Reconstruction to Form Crystalline CuO on Cu_9S_5; and Bulk Reconstruction to Form Crystalline Cu_2O along with Amorphous CuO

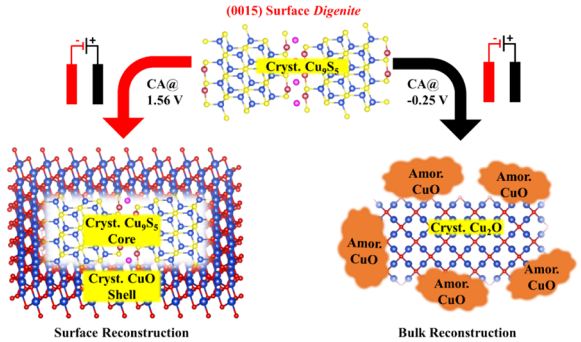

In order to validate the formation of Cu(OH) as reactive species for HER from $Cu(OH)_2$ or CuO, these two materials were independently prepared (Figure S28) and their redox chemistry was studied. To compare the redox feature seen for the Cu_9S_5 and CuS and to interpret the most probable HER path, the CV study of $Cu(OH)_2$@NF electrode within the

https://doi.org/10.1021/jacsau.3c00703
JACS Au 2024, 4, 642−656

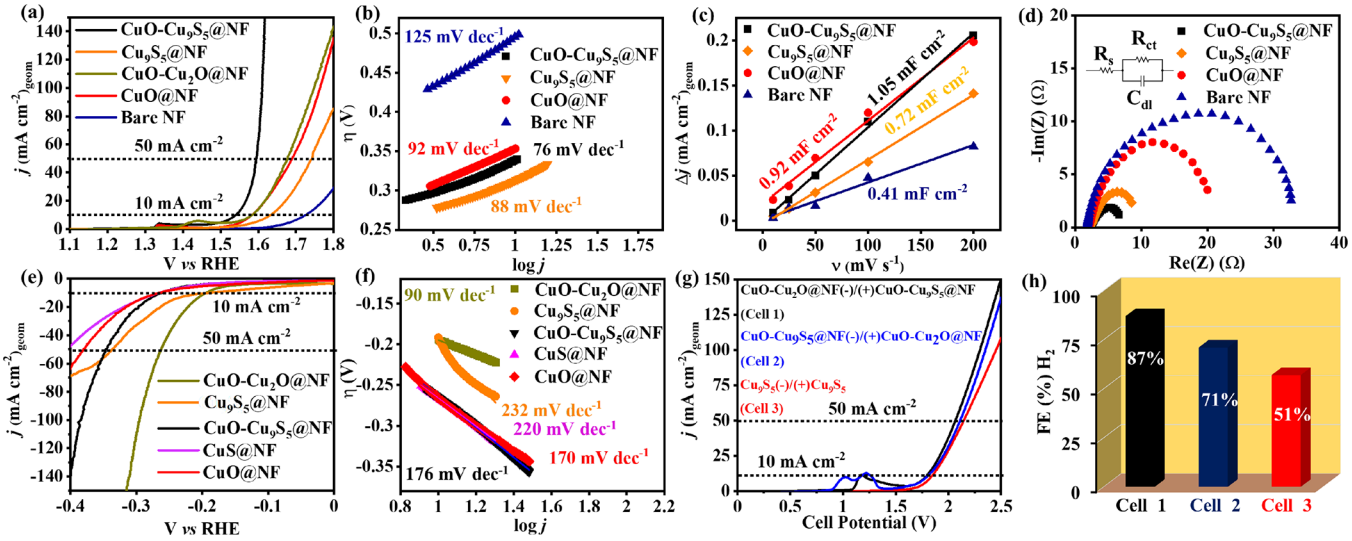

Figure 7. (a) Polarization curves recorded between 1.2 and 1.8 V vs RHE with CuO-Cu_9S_5@NF, Cu_9S_5@NF, CuO-Cu_2O@NF, CuO@NF, and bare NF as working electrodes. (b) Tafel slope from the LSV data. (c) C_{dl} and (d) Nyquist plot (inset: equivalent RC circuit) of CuO-Cu_9S_5@NF, Cu_9S_5@NF, CuO/NF, and bare NF. (e) Polarization curves recorded between 0 and −0.4 V vs RHE. (f) Tafel slope from the LSV curves presented in panel (e) of CuO-Cu_2O@NF, Cu_9S_5@NF, CuO-Cu_9S_5@NF, CuS@NF, and CuO@NF. (g) Polarization curve obtained for the overall water splitting study performed with the cell represented in the inset and (h) corresponding FE of the cell with respect to hydrogen. Electrochemical conditions: polarization curves from LSV study; the scan starts at 1.1 V and moved to 1.8 V for OER; for the HER, the scan starts at 0 V and moved to −0.4 V; scan rate: 1 mV s^{-1}. Pt as the counter electrode, Hg/HgO(1 M NaOH) as the reference electrode, 1 M KOH as electrolyte.

same potential window gave a diffuse redox peak near approximately 82 mV (Figure S29), which is presumably due to the formation of Cu(OH) via one-electron reduction. Cu(OH) may also undergo direct dehydration to give a stable Cu_2O species as detected by ex situ studies. Now, in the anodic scan of the CV study with the $Cu(OH)_2$@NF electrode, two distinct redox peaks can be ascribed the reoxidation of electrogenerated Cu(OH) and Cu_2O (Figure S30). Electrochemical study was also performed with independently prepared CuO. In the CV cycle, the cathodic scan within a potential window −0.1 to 1.0 V showed a broad reduction peak after −0.1 V (Figure S31) and with a crossover in the anodic scan was noticed followed by two dominant redox peaks. In the cathodic scan of the 10th CV cycle of the $Cu(OH)_2$@NF electrode and/or Cu_2O@NF, a catalytic current for the HER after −0.02 V was observed (Figure S32), which is similar to that observed for Cu_9S_5 or CuS. Therefore, Cu(OH) and Cu_2O both can generate under the cathodic conditions and contribute to the HER.

To identify the structural modification of CuS under different electrode conditions, CA studies at two different potentials, namely, 1.56 V and −0.25 V (vs RHE) was done with the CuS/NF electrode (Figure S33). After 4 h of CA in these two extreme potentials, the catalyst was either recovered from the electrode or directly the electrode was characterized. After 4 h of CA at 1.56 V (vs the RHE), the low-magnification FESEM images of the CuS@NF (Figure S34) revealed a structural disintegration of the CuS nanoplate assemblies. Under high magnification, the size and shape of the particles appeared more irregular, losing its characteristic nanoplate morphology. The FESEM-EDX elemental mapping and EDX spectrum depicted some loss of sulfur from the material due to formation of CuO, as reported earlier.[12] The presence of a significant amount of sulfur in the elemental mapping is indicative of partial retention of the CuS structure (Figures S35 and S36). TEM images (Figure S37) further provided evidence in some disintegration of the CuS nanoplate agglomeration. However, high-resolution TEM image on selected nanoplates retained after CA displayed characteristic (006) Bragg's planes with 0.27 nm *d* spacings. In the SAED pattern (Figure S38), the bright spots can be well indexed to (004), (006), and (008) planes (Figure S39), confirming the partial stability of the CuS material under anodic conditions. Raman data of the post-OER material showed characteristic vibrations for CuS at 475 cm^{-1} and CuO at 285−296 cm^{-1}, which is in support of partial deformation (Figure S40). Similar to that of studied under anodic conditions, we also tested under cathodic conditions, and the CA study at −0.25 V versus RHE for 4 h with the CuS@NF electrode (Figure S33) and subsequent FESEM study of the used electrode revealed similar deformation in the individual particles (Figure S41). Furthermore, the EDX elemental mapping and EDX spectrum revealed a partial loss of sulfur and incorporation of oxygen in the structure (Figures S42 and S43). The incorporation of oxygen could be well-ascribed to the formation of CuO as it can be detected in the Raman spectrum (Figure S44). Notably, in TEM images (Figure S45), some CuS nanoplates were identified along with the formation of flakes. However, the HRTEM image can identify the Braggs planes (101), (008), and (108) corresponding to the 0.32, 0.20, and 0.17 nm *d*-spacing values (Figure S46). In the SAED pattern (Figure S47), the same lattice planes were identified as bright diffractions. Although a partial structural deformation was observed for CuS nanoplates under both anodic and cathode conditions, it is relatively stable compared to the Cu_9S_5 particles.

Electrocatalytic Water Splitting

As noted during electrochemical CV cycles and CA study, there is an alteration of the Cu_9S_5 structure to evolve oxidic phases. This feature is indeed observed in most of the metal chalcogenide during alkaline electrocatalysis.[37,38,41] The

https://doi.org/10.1021/jacsau.3c00703
JACS Au 2024, 4, 642−656

structural alteration however favors the electrochemical activity and often supersedes the independently prepared metal oxide. The same has been noticed with covellite CuS, where during the CV cycles within a potential window of 1.0 to 1.7 V, and tenorite CuO evolves and acted as a true catalyst to facilitate the OER. Herein, Cu_9S_5 also transformed to CuO-Cu_9S_5 under the +1.56 V CA conditions, and during the CA within 2 h, the current reaches a maximum value. This is a clear indication that the in situ-evolved CuO-Cu_9S_5 is more reactive compared to pristine Cu_9S_5. On the other hand, a complete alteration of Cu_9S_5 to a mixture of amorphous CuO and crystalline Cu_2O was noticed under −0.25 V CA. Notably the initial current fluctuations in the CA curve were a clear indication of the sulfide leaching and structural modification. Under −0.25 V CA conditions, the current delivered over the last 3 h was higher than the initial value. Therefore, in situ-formed Cu_xO under a cathodic potential possesses better catalytic activity. As a consequence, two individual half-cell reactions were tested with the pristine and in situ modified samples obtained from the CA under two different polarities.

The OER activity was checked with the pristine Cu_9S_5, the in situ-modified CuO-Cu_9S_5 and independently prepared CuO samples deposited on the NF substrate and using 1 M KOH as electrolyte. Polarization curves obtained from the liner sweep voltammetry (LSV) study depicted a difference in activity of these three samples. For CuO-Cu_9S_5@NF, on sweeping the potential, the current density started increasing rapidly, and after 1.51 V, the current has exponentially grown up to 150 mA cm^{-2} at 1.6 V. The polarization curve provided 308, 360, and 380 mV overpotential values at current densities of 10, 50, and 100 mA cm^{-2}, respectively (Figure 7a). Under the similar condition, Cu_9S_5@NF showed moderate activity and delivered a current density of 100 mA cm^{-2} at 1.8 V with an overpotential of 400 mV. It could be noted that Cu_9S_5 prepared via the SSP approach reported by Driess et al. also possesses a core−shell CuO@Cu_9S_5 structure after 12 h, and the Cu_9S_5 on NF was able to deliver a comparable activity with 368 mV (Table S1) overpotential at 50 mA cm^{-2}.[18] In a very similar condition, Cu_2S also showed comparable activity.[49] However, the independently prepared CuO could only achieve a current density of 50 mA cm^{-2} overpotential of 460 mV (Figure 7a), depicting inferior activity with respect to the CuO-Cu_9S_5. Under the similar electrochemical condition, the in situ-formed amor-CuO/cryst-Cu_2O@NF (denoted as CuO-Cu_2O@NF) from the pristine Cu_9S_5@NF (under CA at −0.25 V) achieved an overpotential of 458 mV. The fair activity of the CuO-Cu_9S_5@NF can be correlated to the better kinetics as evident from the Tafel slope[50] of 76 mV dec^{-1} (Figure 7b). The Cu_9S_5@NF and CuO@NF electrode gave a Tafel slope of 88 and 92 mV dec^{-1}, respectively (Figure 7b). The double-layer capacitance (C_{dl}) was further determined with the electrodes to correlate the activity with the number of surface-active sites available in the catalyst deposited on NF. The electrochemical surface area (ECSA) is directly related to the number of active sites, and it can be calculated from the experimentally determined C_{dl} value (Figure S48). For CuO-Cu_9S_5, the C_{dl} was determined to be 1.05 mF cm^{-2}, which is higher than that obtained for Cu_9S_5 (0.72 mF cm^{-2}) and CuO (0.92 mF cm^{-2}) (Figure 7c). The calculated ECSA for CuO-Cu_9S_5 was 0.62 cm^2, which is larger than that of Cu_9S_5 (ECSA of 0.54 cm^2). Therefore, it is clear that the structural alteration of Cu_9S_5 at 1.56 V CA resulted in an exposed surface with more available active sites. To ensure the intrinsic activity of the CuO-Cu_9S_5@NF anode, other electrochemical metrics such as the turnover frequency (TOF), mass activity, and exchange current density (j_0') was calculated. At an overpotential of 350 mV, the mass activity was 5.9 A g^{-1} and TOF was 0.011 s^{-1}, which are considerably better than the reported value with copper-based anodes.[12,14] The exchange current density of 0.8 mA cm^{-2} for the CuO-Cu_9S_5@NF anode was as comparable as the previously reported benchmark IrO_2.[51] Moreover, the charge-transfer resistance (R_{ct}) calculated to be 4.9 Ω from the semicircular Nyquist plot obtained from the electrochemical impedance study with CuO-Cu_9S_5 reflected better electrode−electrolyte interface charge transfer kinetics (Figure 7d).[52] From the R_{ct} value (7.8 Ω) obtained for pristine Cu_9S_5, it was evident that CuO layer formation on the Cu_9S_5 favors the charge transfer during electrocatalysis. It could further be noted that the CuO@NF delivered a higher R_{ct} of 18.9 Ω. Therefore, the Cu_9S_5 core plays an intriguing role in controlling the electrokinetics.[53] Literature study highlighted that metal sulfides favor electron conductivity.[54] Based on the electrochemical data, it is now evident that electro-modification of Cu_9S_5 structure however helped to improve the activity, providing a reactive CuO shell on top of the Cu_9S_5. During the CV cycles with Cu_9S_5, the $Cu^{III/II}$ redox feature was noticeable, which indicates Cu^{III} to be the reactive species for the OER.[20] Also, the activated electrode remained stable for over 10 h of long-term operation delivering a stable current density (Figure S49). After 3.5 h of CA, a small increment (2 mA cm^{-2}) in the current density was presumably due to a complete structural alteration of the residual Cu_9S_5 present in the CuO@Cu_9S_5. To prove further the long-term stability of the CuO-Cu_9S_5@NF, continuous CV cycles were recorded within the potential of 0.9−2.1 V in a three-electrode set up. There was an insignificant drop in the current density in the 200th CV cycle compared to the first CV cycle, confirming the stability of the electrode (Figure S50). The long-term OER performance was ensured by performing CA at 1.56 V for 10 h and LSV study with the used electrode showing a slight drop in the current density (Figure S51). The post-CA PXRD pattern of the isolated powder sample revealed strong reflection of (11−1), (111), and (220) planes corresponding to the CuO phase with some residual weak reflections of the (0015) plane of Cu_9S_5 (Figure S52). Dominant peaks at 44.8° and 52.3° were due to metallic nickel from the NF used as support. FESEM images (Figure S53) portrayed complete morphological changes of the Cu_9S_5 particles. A high oxygen percentage was detected by both the EDX and elemental mapping (Figures S54 and S55), which indicated leaching of sulfur and formation CuO. Some residual sulfur could be due to the surface re-adsorbed sulfate anions. Low-magnification TEM images (Figure S56) also supported the structural deformation of the pristine crystalline particles to irregular shapes. The lattice fringes obtained from the HRTEM images with interplanar spacing of 0.18, 0.15, and 0.13 nm matched well with the crystal planes of (20−2), (202), and (220), respectively, of the CuO phase (Figure S57). The SAED pattern indicated a strong crystalline nature of the CuO showing diffraction rings for (111), (20−2), and (202) planes (Figure S58). Core-level Cu 2p XPS spectra recorded from the isolated powder sample after CA, indicated Cu^{II} as dominant species in the post-CA sample (Figure S59). The core-level S 2p XP spectrum could be well correlated to the formation of the sulfate anion with a S−O peak at 168.2 eV (Figure S59). Deconvolution of the O 1s XP spectrum indicated the

https://doi.org/10.1021/jacsau.3c00703
JACS Au 2024, 4, 642−656

presence of O^{2-} and OH^-. Post-CA characterization data indicated that the formation of crystalline CuO. The presence of amorphous $Cu(OH)_2$ along with CuO is highly likely.

The in situ-formed amor-CuO/cryst-Cu_2O@NF (denoted as CuO-Cu_2O@NF) from the pristine Cu_9S_5@NF was found to be the best cathode to show promising HER activity in alkaline medium. The polarogram recorded within the potential window of 0 to −0.4 V with the CuO-Cu_2O@NF electrode provided overpotentials of 190, 216, and 226 mV at current densities of −5, −10, and −20 mA cm^{-2}, respectively (Figure 7e). Under similar electrochemical conditions, a Cu_9S_5@NF electrode showed less reactivity as evident from the polarization curve (Figure 7e). Under the same condition, covellite CuS deposited on NF (denoted as CuS@NF) was apparently inactive. The Cu_9S_5@NF electrode could deliver a cathodic current density of 50 mA cm^{-2} at a 340 mV overpotential, while the CuS@NF electrode with exposed Cu^{2+} sites require a 400 mV overpotential to reach the similar current density. In this direction, in an earlier study with Cu_9S_5, under an applied potential, it gradually changed to Cu_2O. The active species Cu_2O formed from Cu_9S_5 only at a higher potential of −1 V versus RHE, revealing better activity over the electrodes activated under different potentials (Table S2). In comparison to 216 mV reported herein, a previously reported electrode activated at −1 V vs RHE delivered a high overpotential of 263 mV for 10 mA cm^{-2}.[28] The activity of CuO-Cu_9S_5@NF and CuO@NF was also tested in a similar condition and found to have high overpotentials of 275 and 268 mV, respectively, for a 10 mA cm^{-2} current density. Based on recent study, to overcome the interference of dissolved Pt from the Pt counter electrode in HER activity of the CuO-Cu_2O@NF electrode, a control study with a graphite counter electrode was performed. The LSV curve provided an overpotential of 220 mV to achieve a current density 10 mA cm^{-2} (Figure S60). Changing the Pt counter electrode to graphite rod did not show any effect in the HER activity. These data established firmly that the HER activity of the catalysts is solely due to copper present in the material and not due to re-adsorption of the dissolved Pt from the counter electrode.[55]

The better activity−kinetics relation for HER activity was established from the lower Tafel slope of the active electrode.[56,57] The activated electrode had a Tafel slope of only 90 mV dec^{-1} (Figure 7f), while the pristine electrode delivered a high Tafel slope of 232 mV dec^{-1}. In comparison to the mixed-valence Cu_9S_5, the mixed valence CuS gave a Tafel slope of 176 mV dec^{-1}. Compared to these, the CuO-Cu_9S_5@NF and CuO@NF gave a ca. Tafel slope of 220 and 170 mV dec^{-1}, respectively. Therefore, like the OER activity, the HER activity too delivered better kinetics well correlated to the higher activity of the active electrode. For long-term stability, the CA study at a constant potential of −0.25 V vs RHE revealed a constant current density over −5 mA cm^{-2} for about 15 h (Figure S61). To affirm a prolonged stability and performance of the CuO-Cu_2O@NF, 200 CV cycles were recorded within a potential window of 0.5 to −0.7 V and there was small drop in the current response in the 200th CV scan compared to the first scan (Figure S62). Similarly, a small drop in the current was noticed when LSV recorded with the CuO-Cu_2O@NF electrode recovered after 15 h CA at −0.25 V (Figure S63). To understand the structural and chemical alteration, CA-HER (at −0.25 V) was performed for 15 h and the postcatalytic samples were either isolated from the electrode and/or directly characterized on the electrode surface. The PXRD data provided concrete evidence in support of the existence of the crystalline Cu_2O phase (Figure S64). After HER-CA, the FESEM images (Figure S65) acquired on the electrode surface revealed some structural alteration of the well-defined nanocubes. The EDX elemental mapping (Figures S66 and S67) performed on the electrode provided an intense signal for oxygen with some residual sulfur species, which was presumably due to re-adsorption of the leached sulfur in the form of sulfate anions. TEM images (Figure S68) also pointed out the morphological alteration as detected through FESEM. HR-TEM study provided an atomic resolution image, which identified two distinct lattice fringes of 0.24 and 0.21 nm corresponding to (111) and (200) planes of the crystalline Cu_2O phase (Figure S69). The SAED pattern also supported the Cu_2O phases with bright diffraction spots of (111), (200), and (220) planes (Figure S70). The surface composition of the post-catalytic sample was further studied where core-level Cu 2p XPS indicated Cu^I species to be predominant, which is also identical to that observed after the 4 h CA study (Figure S71). In the core-level S 2p envelop, the strong S−O bond indicated the presence of a surface-adsorbed sulfate anion, which is in-line with the presence of a large amount of oxygen detected in the EDX-elemental mapping. Post-HER CA study thereby evidences Cu_2O as the dominant electroactive species that persists on the electrode in the long-term HER conditions.

Due to considerable HER and OER performance of the electrochemically modified electrodes, the activated electrodes were coupled to construct an electrolyzer for overall water splitting (OWS). As the performance of the electro-modified catalysts have shown better activity toward individual half-cell reactions, they were chosen as cathode and anode to fabricate the two-electrode single compartment cell as an electrolyzer. In this context, CuO-Cu_2O@NF as a cathode and CuO-Cu_9S_5@NF as an anode were coupled together to build the cell CuO-Cu_2O@NF(−)/(+)CuO-Cu_9S_5@NF and to test the performance, LSV was recorded using 1 M KOH as the electrolyte, keeping a sweep rate of 1 mV s^{-1}. The polarization curve recorded with the cell provided a high current output of 150 mA cm^{-2} at a high cell potential of 2.5 V. A cell potential of 1.79 and 2.0 V was recorded to deliver a current density of 10 mA and 50 mA cm^{-2}, respectively (Figure 7g). In the similar electrochemical conditions, when the electrodes were replaced with the pristine catalyst, the Cu_9S_5(−)/(+)Cu_9S_5 cell required a 1.86 V cell potential to depict a current density of 10 mA cm^{-2}. To realize the efficiency of the cell to produce green hydrogen via water electrolysis, hydrogen evolved by the cathode was quantified by gas chromatography (GC). The electrolyzer CuO-Cu_2O@NF(−)/(+)CuO-Cu_9S_5@NF (cell 1) remained better in generating more hydrogen compared to the CuO-Cu_9S_5@NF(−)/(+)CuO-Cu_2O@NF (cell 2) and Cu_9S_5(−)/(+)Cu_9S_5 cell (cell 3). For the first one, the Faradaic efficiency (FE) for H_2 production was recorded to be 87(±3) %, while the third cell with pristine electrodes was able to provide a FE of only 51(±3) % (Figure 7h, Figures S72−S75, and Table S3). However, switching the electrode terminals of cell 1 to obtain cell 2 resulted drop in FE by 16% (Figure 7h and Figure S74). The lower FE with the pristine electrode was due to the consumption of a large amount of electrical charge for the reconstruction of the Cu_9S_5 pre-catalyst to electroactive oxidic species. Once the catalyst on the electrode surface is modified, the remaining charge passed through the electrode are being utilized for water splitting.

https://doi.org/10.1021/jacsau.3c00703
JACS Au 2024, 4, 642−656

Under the similar condition, other cell setups with other possible combinations did not stand as better choice as confirmed from the respective LSV curves where a high cell potential is required to deliver a comparable density (Figure 7g). Therefore, in situ electro-modified catalyst on NF are the best choice for constructing an efficient electrolyzer to split water to generate green hydrogen with pronounced electrochemical efficiency.

CONCLUSIONS

Two analogous copper sulfide Cu_9S_5 and CuS were prepared solvothermally and the nanoscale particles were characterized by several spectroscopic and microscopic studies. The mixed-valence state of copper in both structure was confirmed by Cu 2p XPS. The exposed surface of the rhombohedral Cu_9S_5 and hexagonal CuS lattice was identified in the HRTEM. The atomic arrangement of the (0015) surface and (002) surface of Cu_9S_5 and CuS was found to be significantly different despite both containing mixed-valence copper ions. The (0015) surface consisted of mostly T_d Cu^{II} along with some T_p Cu^{I} and a limited number of O_h Cu^{II} sites, which make it a divergent surface. The (002) surface of CuS is formed by T_d $Cu^{II}S_4$ repeating units and possess a homogeneity. During the electrochemical study, the surface disparity of these two mixed valence copper sulfides was reflected in their redox behavior. The wettability test and contact angle measurement highlighted a difference in the surface energy of Cu_9S_5 and CuS. BET study also inferred a rougher surface of Cu_9S_5 particles. Both showed distinct $Cu^{II/I}$ redox, although potentials were distinct due to the difference in the Cu^{II} to Cu^{I} ratio and their distribution in the exposed surface. However, quasi in situ Raman study pointed out that, during the CV cycles within −0.1 to 1.6 V, the Cu_9S_5 surface appeared to be labile and CuO formed as an overlayer. During reduction conditions, CuS appeared relatively more stable, while with CV cycles in the anodic region, that is, 1 to 1.6 V, a slow degradation was noticed. Post-anodic CA and ex situ analyses of the Cu_9S_5@NF anode revealed a surface corrosion, while under CA, at the cathodic potential, complete breakdown of Cu_9S_5 was noticed. In situ Raman study also found out the CuO_x formation under two different potential ranges. The electro-modification of Cu_9S_5 however helped in obtaining a more active CuO_x catalyst for individual half-cell reactions' of the OER and HER, and the activity is superior to CuO_x formed from CuS or independently prepared CuO. An OWS electrolyzer was then fabricated with the modified electrodes to obtain a better cell potential and higher Faradaic efficiency. This study comprehensively showcased the role of surface-active sites in controlling electrochemical behavior of mixed valence copper sulfides and correlate their electrochemical stability with the lattice structure. Further, the structural evolution and the active species formation pathway are concisely presented which provides a clear understanding about the electrocatalysis performed herein and/or earlier in literature. It turns out that copper sulfide with a higher exposed surface structure facilitates faster in situ electrochemical reconstruction to surface active oxide/hydroxide species, giving rise to better electrocatalytic activity. The structural lability of the copper sulfides could also be interpreted from the lattice structure and atomic arrangements in the exposed surface. This study highlighted that homogeneity in the exposed surfaces results in reactive and high surface energy with better electrolyte diffusion and it could also be a reason to show better electrochemical activity. Despite some recent literatures discussing the surface reconstruction, identifying the reactive species via post-characterization after electrocatalysis, the plausible interpretation of electrochemical reactivity considering the surface energy of the exposed facets and detailed lattice analyses with atomic arrangements studied herein could be a uniform approach to correlate the structure to the activity of the metal chalcogenides.

ASSOCIATED CONTENT

Supporting Information

The Supporting Information is available free of charge at https://pubs.acs.org/doi/10.1021/jacsau.3c00703.

Characterization of the catalysts by spectroscopic, microscopic, PXRD and analytical techniques along with the details of the experimental and electrochemical methods (PDF)

AUTHOR INFORMATION

Corresponding Author

Biswarup Chakraborty − *Department of Chemistry, Indian Institute of Technology Delhi, New Delhi 110016, India;* orcid.org/0000-0002-6292-6357; Email: cbiswarup@chemistry.iitd.ac.in

Author

Avinava Kundu − *Department of Chemistry, Indian Institute of Technology Delhi, New Delhi 110016, India*

Complete contact information is available at: https://pubs.acs.org/10.1021/jacsau.3c00703

Author Contributions

CRediT: **Avinava Kundu** data curation, formal analysis, investigation, methodology, writing-original draft; **Biswarup Chakraborty** conceptualization, formal analysis, funding acquisition, investigation, project administration, resources, supervision, validation, visualization, writing-review & editing.

Notes

The authors declare no competing financial interest.

ACKNOWLEDGMENTS

A.K. acknowledges DST INSPIRE for fellowship [IF190978]. B.C. sincerely acknowledges DST INSPIRE Faculty research grant no. DST/INSPIRE/04/2019/001547. The authors thank Prof. Leena Nebhani and Lukkumanul Hakkim N. from the Department of Materials Science and Engineering, IIT Delhi, for their generous support to measure the contact angles.

REFERENCES

(1) Chen, L.; Chen, Y.-B.; Wu, L.-M. Synthesis of Uniform Cu_2S Nanowires from Copper−Thiolate Polymer Precursors by a Solventless Thermolytic Method. *J. Am. Chem. Soc.* **2004**, *126* (50), 16334−16335.

(2) Evans, H. T. Djurleite ($Cu_{1.94}S$) and Low Chalcocite (Cu_2S): New Crystal Structure Studies. *Science* **1979**, *203* (4378), 356−358.

(3) Itzhak, A.; Teblum, E.; Girshevitz, O.; Okashy, S.; Turkulets, Y.; Burlaka, L.; Cohen-Taguri, G.; Shawat Avraham, E.; Noked, M.; Shalish, I.; Nessim, G. D. Digenite (Cu_9S_5): Layered p-Type Semiconductor Grown by Reactive Annealing of Copper. *Chem. Mater.* **2018**, *30* (7), 2379−2388.

(4) Wen, Y.; Fang, N.; Liu, W.; Yang, T.; Xu, Y.; Huang, X. Cu_7S_4 Nanosheets Enriched with Cu−S Bond for Highly Active and Selective CO_2 Electroreduction to Formate. *J. Mater. Chem. A* **2023**, *11* (20), 10823−10827.
(5) Wang, W.; Cheng, X.; Liao, J.; Lin, Z.; Chen, L.; Liu, D.; Zhang, T.; Li, L.; Lu, Y.; Xia, H. Synergistic Photothermal and Photodynamic Therapy for Effective Implant-Related Bacterial Infection Elimination and Biofilm Disruption Using Cu_9S_8 Nanoparticles. *ACS Biomater. Sci. Eng.* **2019**, *5* (11), 6243−6253.
(6) Gotsis, H. J.; Barnes, A. C.; Strange, P. Experimental and Theoretical Investigation of the Crystal Structure of CuS. *J. Phys.: Condens. Matter* **1992**, *4* (50), 10461.
(7) Xie, Y.; Riedinger, A.; Prato, M.; Casu, A.; Genovese, A.; Guardia, P.; Sottini, S.; Sangregorio, C.; Miszta, K.; Ghosh, S.; Pellegrino, T.; Manna, L. Copper Sulfide Nanocrystals with Tunable Composition by Reduction of Covellite Nanocrystals with Cu^+ Ions. *J. Am. Chem. Soc.* **2013**, *135* (46), 17630−17637.
(8) Gaspari, R.; Manna, L.; Cavalli, A. A Theoretical Investigation of the (0001) Covellite Surfaces. *J. Chem. Phys.* **2014**, *141* (4), 044702.
(9) Peng, Z.; Li, S.; Weng, M.; Zhang, M.; Xin, C.; Du, Z.; Zheng, J.; Pan, F. First-Principles Study of Cu_9S_5: A Novel p-Type Conductive Semiconductor. *J. Phys. Chem. C* **2017**, *121* (42), 23317−23323.
(10) Liang, W.; Whangbo, M. H. Conductivity Anisotropy and Structural Phase Transition in Covellite CuS. *Solid State Commun.* **1993**, *85* (5), 405−408.
(11) Wang, Y.; Feng, X.; Xiong, Y.; Stoupin, S.; Huang, R.; Zhao, M.; Xu, M.; Zhang, P.; Zhao, J.; Abruña, H. D. An Innovative Lithium Ion Battery System Based on a Cu_2S Anode Material. *ACS Appl. Mater. Interfaces* **2020**, *12* (15), 17396−17405.
(12) Kundu, A.; Adak, M. K.; Kumar, Y.; Chakraborty, B. Electrochemically Derived Crystalline CuO from Covellite CuS Nanoplates: A Multifunctional Anode Material. *Inorg. Chem.* **2022**, *61* (12), 4995−5009.
(13) Baláž, M.; Augustyniak, A.; Tatykayev, B.; Shalabayev, Z.; Burashev, G.; Dutková, E.; Daneu, N.; Briančin, J.; Balážová, Ľ.; Tkáčiková, Ľ.; Stahorský, M.; Achimovičová, M.; Baláž, P. Mechanochemical Synthesis of Non-stoichiometric Copper Sulfide $Cu_{1.8}S$ Applicable as a Photocatalyst and Antibacterial Agent and Synthesis Scalability Verification. *Faraday Discuss.* **2023**, *241* (0), 367−386.
(14) Rajput, A.; Kundu, A.; Chakraborty, B. Recent Progress on Copper-Based Electrode Materials for Overall Water-Splitting. *ChemElectroChem.* **2021**, *8* (10), 1698−1722.
(15) Kannimuthu, K.; Sangeetha, K.; Sam Sankar, S.; Karmakar, A.; Madhu, R.; Kundu, S. Investigation on Nanostructured Cu-based Electrocatalysts for Improvising Water Splitting: A Review. *Inorg. Chem. Front.* **2021**, *8* (1), 234−272.
(16) Liu, M.; Liu, Y.; Gu, B.; Wei, X.; Xu, G.; Wang, X.; Swihart, M. T.; Yong, K.-T. Recent Advances in Copper Sulphide-based Nanoheterostructures. *Chem. Soc. Rev.* **2019**, *48* (19), 4950−4965.
(17) Chandrasekaran, S.; Yao, L.; Deng, L.; Bowen, C.; Zhang, Y.; Chen, S.; Lin, Z.; Peng, F.; Zhang, P. Recent Advances in Metal Sulfides: from Controlled Fabrication to Electrocatalytic, Photocatalytic and Photoelectrochemical Water Splitting and Beyond. *Chem. Soc. Rev.* **2019**, *48* (15), 4178−4280.
(18) Chakraborty, B.; Kalra, S.; Beltrán-Suito, R.; Das, C.; Hellmann, T.; Menezes, P. W.; Driess, M. A Low-Temperature Molecular Precursor Approach to Copper-Based Nano-Sized Digenite Mineral for Efficient Electrocatalytic Oxygen Evolution Reaction. *Chem.—Asian J.* **2020**, *15* (6), 852−859.
(19) Deng, Y.; Handoko, A. D.; Du, Y.; Xi, S.; Yeo, B. S. In Situ Raman Spectroscopy of Copper and Copper Oxide Surfaces during Electrochemical Oxygen Evolution Reaction: Identification of Cu^{III} Oxides as Catalytically Active Species. *ACS Catal.* **2016**, *6* (4), 2473−2481.
(20) Zuo, Y.; Liu, Y.; Li, J.; Du, R.; Han, X.; Zhang, T.; Arbiol, J.; Divins, N. J.; Llorca, J.; Guijarro, N.; Sivula, K.; Cabot, A. In Situ Electrochemical Oxidation of Cu_2S into CuO Nanowires as a Durable and Efficient Electrocatalyst for Oxygen Evolution Reaction. *Chem. Mater.* **2019**, *31* (18), 7732−7743.
(21) Umapathi, S.; Singh, H.; Masud, J.; Nath, M. Nanostructured Copper Selenide as an Ultrasensitive and Selective Non-enzymatic Glucose Sensor. *Mater. Adv.* **2021**, *2* (3), 927−932.
(22) Kim, H. S.; Choi, J.; Kong, J.; Kim, H.; Yoo, S. J.; Park, H. S. Regenerative Electrocatalytic Redox Cycle of Copper Sulfide for Sustainable NH_3 Production under Ambient Conditions. *ACS Catal.* **2021**, *11* (1), 435−445.
(23) Ji, L.; Li, L.; Ji, X.; Zhang, Y.; Mou, S.; Wu, T.; Liu, Q.; Li, B.; Zhu, X.; Luo, Y.; Shi, X.; Asiri, A. M.; Sun, X. Highly Selective Electrochemical Reduction of CO_2 to Alcohols on an FeP Nanoarray. *Angew. Chem., Int. Ed.* **2020**, *59* (2), 758−762.
(24) Lang, R.; Li, T.; Matsumura, D.; Miao, S.; Ren, Y.; Cui, Y.-T.; Tan, Y.; Qiao, B.; Li, L.; Wang, A.; Wang, X.; Zhang, T. Hydroformylation of Olefins by a Rhodium Single-Atom Catalyst with Activity Comparable to $RhCl(PPh_3)_3$. *Angew. Chem., Int. Ed.* **2016**, *55* (52), 16054−16058.
(25) Yin, A.-X.; Min, X.-Q.; Zhang, Y.-W.; Yan, C.-H. Shape-Selective Synthesis and Facet-Dependent Enhanced Electrocatalytic Activity and Durability of Monodisperse Sub-10 nm Pt−Pd Tetrahedrons and Cubes. *J. Am. Chem. Soc.* **2011**, *133* (11), 3816−3819.
(26) de Gennes, P. G. Wetting: Statics and Dynamics. *Rev. Mod. Phys.* **1985**, *57* (3), 827−863.
(27) Das, J.; Mandal, S.; Borbora, A.; Rani, S.; Tenjimbayashi, M.; Manna, U. Modulating Force of Nucleated Hydrogen Bubble Adhesion to Boost Electrochemical Water Splitting. *Adv. Funct. Mater.* **2023**, 2311648.
(28) Liang, C.; Li, X.; Han, J.; Ye, N.; Liu, H.; Feng, H.; Huang, L.; Liu, Y.; Peng, X. Hierarchical Cu/Cu_2O Structure Derived from Hexagonal Cu_9S_5 Nanocrystal with Enhanced Electrocatalytic Ability for Hydrogen Evolution Reaction. *J. Alloys Compd.* **2021**, *883*, 160816.
(29) Paliwal, A.; Bandas, C. D.; Thornburg, E. S.; Haasch, R. T.; Gewirth, A. A. Enhanced Nitrate Reduction Activity from Cu-Alloy Electrodes in an Alkaline Electrolyte. *ACS Catal.* **2023**, *13* (10), 6754−6762.
(30) Masa, J.; Sinev, I.; Mistry, H.; Ventosa, E.; de la Mata, M.; Arbiol, J.; Muhler, M.; Roldan Cuenya, B.; Schuhmann, W. Ultrathin High Surface Area Nickel Boride (Ni_xB) Nanosheets as Highly Efficient Electrocatalyst for Oxygen Evolution. *Adv. Energy Mater.* **2017**, *7* (17), 1700381.
(31) Anantharaj, S.; Sugime, H.; Yamaoka, S.; Noda, S. Pushing the Limits of Rapid Anodic Growth of $CuO/Cu(OH)_2$ Nanoneedles on Cu for the Methanol Oxidation Reaction: Anodization pH Is the Game Changer. *ACS Appl. Energy Mater.* **2021**, *4* (1), 899−912.
(32) Elgrishi, N.; Rountree, K. J.; McCarthy, B. D.; Rountree, E. S.; Eisenhart, T. T.; Dempsey, J. L. A Practical Beginner's Guide to Cyclic Voltammetry. *J. Chem. Educ.* **2018**, *95* (2), 197−206.
(33) Piñeiro-García, A.; Wu, X.; Rafei, M.; Mörk, P. J.; Gracia-Espino, E. A Quaternary Mixed Oxide Protective Scaffold for Ruthenium During Oxygen Evolution Reaction in Acidic Media. *Commun. Eng.* **2023**, *2* (1), 28.
(34) Enman, L. J.; Vise, A. E.; Burke Stevens, M.; Boettcher, S. W. Effects of Metal Electrode Support on the Catalytic Activity of Fe(oxy)hydroxide for the Oxygen Evolution Reaction in Alkaline Media. *ChemPhysChem* **2019**, *20* (22), 3089−3095.
(35) Karastogianni, S.; Girousi, S. Electrochemical Behavior and Voltammetric Determination of a Manganese(II) Complex at a Carbon Paste Electrode. *Anal. Chem. Insights* **2016**, *11*, ACI.S32150.
(36) Fang, Z.; Zhang, P.; Wang, M.; Li, F.; Wu, X.; Fan, K.; Sun, L. Selective Electro-oxidation of Alcohols to the Corresponding Aldehydes in Aqueous Solution via Cu(III) Intermediates from CuO Nanorods. *ACS Sustainable Chem. Eng.* **2021**, *9* (35), 11855−11861.
(37) Kundu, A.; Kumar, B.; Chakraborty, B. Greigite Fe_3S_4-Derived α-FeO(OH) Promotes Slow O−O Bond Formation in the Second-

https://doi.org/10.1021/jacsau.3c00703
JACS Au 2024, 4, 642−656

Order Oxygen Evolution Reaction Kinetics. *J. Phys. Chem. C* **2022**, *126* (38), 16172−16186.
(38) Gao, L.; Cui, X.; Sewell, C. D.; Li, J.; Lin, Z. Recent Advances in Activating Surface Reconstruction for the High-efficiency Oxygen Evolution Reaction. *Chem. Soc. Rev.* **2021**, *50* (15), 8428−8469.
(39) Wygant, B. R.; Kawashima, K.; Mullins, C. B. Catalyst or Precatalyst? The Effect of Oxidation on Transition Metal Carbide, Pnictide, and Chalcogenide Oxygen Evolution Catalysts. *ACS Energy Lett.* **2018**, *3* (12), 2956−2966.
(40) Peters, E.; Majima, H. Electrochemical Reactions of Pyrite in Acid Perchlorate Solutions. *Can. Metall. Q.* **1968**, *7* (3), 111−117.
(41) Kundu, A.; Kumar, B.; Rajput, A.; Chakraborty, B. Integrating Electrochemical CO_2 Reduction on α-NiS with the Water or Organic Oxidations by Its Electro-Oxidized NiO(OH) Counterpart to an Artificial Photosynthetic Scheme. *ACS Appl. Mater. Interfaces* **2023**, *15* (6), 8010−8021.
(42) Mushtaq, N.; Wang, Z.; Tabassum, H.; Tahir, M.; Han, Z.; Zhu, Y.; Younas, W.; Ma, X.; Cao, C. A Facile and Simple Microwave-assisted Synthesis Method for Mesoporous Ultrathin Iron Sulfide Nanosheets as an Efficient Bifunctional Electrocatalyst for Overall Water Splitting. *Dalton Trans.* **2022**, *51* (16), 6285−6292.
(43) Anantharaj, S.; Nagamatsu, T.; Yamaoka, S.; Li, M.; Noda, S. Efficient Methanol Electrooxidation Catalyzed by Potentiostatically Grown Cu−O/OH(Ni) Nanowires: Role of Inherent Ni Impurity. *ACS Appl. Energy Mater.* **2022**, *5* (1), 419−429.
(44) Ao, X.; Gu, Y.; Li, C.; Wu, Y.; Wu, C.; Xun, S.; Nikiforov, A.; Xu, C.; Jia, J.; Cai, W.; Ma, R.; Huo, K.; Wang, C. Sulfurization-functionalized 2D Metal-organic Frameworks for High-performance Urea Fuel Cell. *Appl. Catal., B* **2022**, *315*, 121586.
(45) Sun, H.; Li, L.; Chen, H.-C.; Duan, D.; Humayun, M.; Qiu, Y.; Zhang, X.; Ao, X.; Wu, Y.; Pang, Y.; Huo, K.; Wang, C.; Xiong, Y. Highly Efficient Overall Urea Electrolysis via Single-atomically Active Centers on Layered Double Hydroxide. *Sci. Bull.* **2022**, *67* (17), 1763−1775.
(46) Wang, Y.-H.; Zheng, S.; Yang, W.-M.; Zhou, R.-Y.; He, Q.-F.; Radjenovic, P.; Dong, J.-C.; Li, S.; Zheng, J.; Yang, Z.-L.; Attard, G.; Pan, F.; Tian, Z.-Q.; Li, J.-F. In situ Raman Spectroscopy Reveals the Structure and Dissociation of Interfacial Water. *Nature* **2021**, *600* (7887), 81−85.
(47) Adams, J. S.; Chemburkar, A.; Priyadarshini, P.; Ricciardulli, T.; Lu, Y.; Maliekkal, V.; Sampath, A.; Winikoff, S.; Karim, A. M.; Neurock, M.; Flaherty, D. W. Solvent Molecules form Surface Redox Mediators In situ and Cocatalyze O_2 Reduction on Pd. *Science* **2021**, *371* (6529), 626−632.
(48) Debbichi, L.; Marco de Lucas, M. C.; Pierson, J. F.; Krüger, P. Vibrational Properties of CuO and Cu_4O_3 from First-Principles Calculations, and Raman and Infrared Spectroscopy. *J. Phys. Chem. C* **2012**, *116* (18), 10232−10237.
(49) Zhao, X.; Liu, L.; Zhang, Y.; Zhang, H.; Wang, Y. Uniquely Confining Cu_2S Nanoparticles in Graphitized Carbon Fibers for Enhanced Oxygen Evolution Reaction. *Nanotechnology* **2017**, *28* (34), 345402.
(50) Saxena, A.; Kapila, S.; Medvedeva, J. E.; Nath, M. Copper Cobalt Selenide as a Bifunctional Electrocatalyst for the Selective Reduction of CO_2 to Carbon-Rich Products and Alcohol Oxidation. *ACS Appl. Mater. Interfaces* **2023**, *15* (11), 14433−14446.
(51) Schuler, T.; Kimura, T.; Schmidt, T. J.; Büchi, F. N. Towards a Generic Understanding of Oxygen Evolution Reaction Kinetics in Polymer Electrolyte Water Electrolysis. *Energy Environ. Sci.* **2020**, *13* (7), 2153−2166.
(52) Chakraborty, B.; Beltrán-Suito, R.; Hausmann, J. N.; Garai, S.; Driess, M.; Menezes, P. W. Enabling Iron-Based Highly Effective Electrochemical Water-Splitting and Selective Oxygenation of Organic Substrates through In Situ Surface Modification of Intermetallic Iron Stannide Precatalyst. *Adv. Energy Mater.* **2020**, *10* (30), 2001377.
(53) Ojha, K.; Saha, S.; Banerjee, S.; Ganguli, A. K. Efficient Electrocatalytic Hydrogen Evolution from MoS_2-Functionalized Mo_2N Nanostructures. *ACS Appl. Mater. Interfaces* **2017**, *9* (23), 19455−19461.
(54) Kulkarni, P.; Nataraj, S. K.; Balakrishna, R. G.; Nagaraju, D. H.; Reddy, M. V. Nanostructured Binary and Ternary Metal Sulfides: Synthesis Methods and Their Application in Energy Conversion and Storage Devices. *J. Mater. Chem. A* **2017**, *5* (42), 22040−22094.
(55) Chen, R.; Yang, C.; Cai, W.; Wang, H.-Y.; Miao, J.; Zhang, L.; Chen, S.; Liu, B. Use of Platinum as the Counter Electrode to Study the Activity of Nonprecious Metal Catalysts for the Hydrogen Evolution Reaction. *ACS Energy Lett.* **2017**, *2* (5), 1070−1075.
(56) Prats, H.; Chan, K. The determination of the HOR/HER Reaction Mechanism from Experimental Kinetic Data. *Phys. Chem. Chem. Phys.* **2021**, *23* (48), 27150−27158.
(57) Panda, C.; Menezes, P. W.; Zheng, M.; Orthmann, S.; Driess, M. In Situ Formation of Nanostructured Core−Shell Cu_3N−CuO to Promote Alkaline Water Electrolysis. *ACS Energy Lett.* **2019**, *4* (3), 747−754.

https://doi.org/10.1021/jacsau.3c00703
JACS Au 2024, 4, 642−656